

## Supporting Information

### **Modeling Carbon-Free Energy Conversion Systems: Enhanced Hydrazine-Assisted Hydrogen Production with Dual-Electric-Field Effect on Needle-like Ru/CoP Catalysts**

Kang Ji,<sup>a</sup> Shiyu Wang,<sup>a</sup> Shuyun Yao,<sup>a</sup> Yingjie Ji,<sup>a</sup> Guixi Wang,<sup>a</sup> Weikun Ren,<sup>a</sup> Jun Wang,<sup>a</sup> Feike Zhang,<sup>a</sup> Jiangzhou Xie,<sup>\*b</sup> Zhiyu Yang,<sup>\*a</sup> Yi-Ming Yan<sup>\*a</sup>

<sup>1</sup> State Key Laboratory of Organic-Inorganic Composites, Beijing Advanced Innovation Center for Soft Matter Science and Engineering, Beijing University of Chemical Technology, Beijing, 100029, People's Republic of China  
<https://orcid.org/0000-0001-5532-7789>

E-mail: yanym22@mail.buct.edu.cn; yangzhiyu@mail.buct.edu.cn

<sup>2</sup> School of Mechanical and Manufacturing Engineering, University of New South Wales, Sydney, New South Wales 2052, Australia

E-mail: jiangzhou.xie@unsw.edu.au

## 1. Experimental section

### 1.1 Synthesis of needle-like Co(OH)F and bulk-like Co(OH)F.

2 mmol of  $\text{Co}(\text{NO}_3)_2 \cdot 6\text{H}_2\text{O}$ , 10 mmol of urea, and 6 mmol  $\text{NH}_4\text{F}$  were dissolved into 60 mL of  $\text{H}_2\text{O}$  and stirred for 0.5 h. Then one piece of pretreated nickel foam (2 cm×4 cm) immersed into the above solution and hydrothermal treatment at 120 °C for 6 h. Finally, the pink nickel foam grown Co(OH)F was obtained by washing with  $\text{H}_2\text{O}$  and drying in vacuum. The bulk-like Co(OH)F was prepared by the same method except for changing the content of  $\text{NH}_4\text{F}$  from 6 to 20 mmol. The treatment of nickel foam was conducted by sonicating in 3.0 M HCl,  $\text{H}_2\text{O}$ , acetone, and ethanol for 0.5 h, respectively.

### 1.2 Synthesis of needle-like Ru/CoP and bulk-like Ru/CoP.

The obtained Co(OH)F was first immersed in 1.0 mM of  $\text{RuCl}_3$  solution at room temperature. After ions exchange for 1 h, the sample was washed with  $\text{H}_2\text{O}$  and dried at 60 °C for one night in vacuum. Finally, 0.3 g of  $\text{NaH}_2\text{PO}_2$  was placed in the upstream of the tube furnace, while the sample was placed in the downstream, and Ru/CoP was obtained after calcination at 350 °C for 2 h in  $\text{N}_2$  atmosphere. The bulk-like Ru/CoP was synthesized by the same steps using bulk Co(OH)F as precursor.

## 2. Characterization

X-ray diffraction patterns were obtained on Rigaku D/max 2500. SEM and TEM images were acquired on SU4800 and HT-7700, respectively. XPS was conducted on Thermo Scientific ESCALAB 250Xi. Raman spectra and in-situ Raman spectra was recorded on (Zolix, China). KPFM image was recorded on Asylum Research MFP-3D.

## 3. Electrochemical measurements.

Electrochemical measurements were performed on Pine Wavedriver bipotentiostat, the prepared electrocatalyst, Ag/AgCl, and carbon rod was served as working electrode, reference electrode and counter electrode. Linear sweep voltammetry (LSV) curves were recorded with a scan rate of 5 mV/s, and the electrocatalyst was activated before testing. Unless otherwise specified, the LSV curves were corrected with 95% and 85% iR-compensation for HER and HzOR, respectively, and the solution resistance was acquired by electrochemical impedance spectroscopy (EIS) measurement. Moreover, EIS plots were measured at a frequency from 0.01 to 1000000 Hz. Electrochemical surface area (ECSA) was obtained by testing cyclic voltammetry (CV) curves at a non-Faradic region, the specific details are listed as follows:

$$\text{ECSA} = C_{\text{dl}}/C_s$$

where  $C_{\text{dl}}$  and  $C_s$  represent double-layer capacitance and specific capacitance, respectively.  $C_{\text{dl}}$  was obtained by CV curves in non-Faradic region, and  $C_s$  value is 0.04 mF/cm<sup>2</sup> in alkaline solution.<sup>1</sup>

In addition, to comprehensively evaluate ECSA, the  $C_{\text{dl}}$  value was obtained by testing EIS plots. The calculation formula is as follows:

$$C = \frac{(Y_0 \times R_p)^{\frac{1}{\alpha}}}{R_p}$$

where  $R_p$  represents the charge transfer resistance, and the value of  $\alpha$  ranges between 0 and 1. When  $\alpha$  approaches 0, it corresponds to a normal resistance, while when  $\alpha$  approaches 1, it corresponds to a normal capacitor.<sup>2</sup>

The TOF values of electrocatalysts were obtained by testing CV curves in 1.0 M PBS solution (scan rate: 50 mV/s, potential windows: 0-0.6 V vs. RHE), every electrocatalyst was tested three times. The specific calculation follows the formula:

$$\text{TOF} = j/2Fn$$

where  $j$ ,  $F$ , and  $n$  represent the current density, Faradic constant (86450), and the number of active sites.

The  $n$  was obtained by the surface charge density ( $Q_s$ ), followed as:

$$n = Q_s/F$$

where  $Q_s$  was half of the charge by integrating CV curves.<sup>3</sup>

### 3.1 Assembly and measurement of OHzS.

The prepared Ru/CoP is used as anode and cathode, and the cathode cavity and anode cavity are separated by anion exchange membrane (Fumasep FAA-3-PK-130). The electrolyte of anode and cathode are respectively 1.0 M KOH+0.3 M N<sub>2</sub>H<sub>4</sub> and 1.0 M KOH. The electrolysis experiment was carried out on PINE, the LSV scanning speed was 5 mV/s, and all curves without iR-compensation. The OHzS test in simulated seawater (0.5 M NaCl solution) is to use seawater instead of pure water as solvent, and other conditions are the same.

### 3.2 Assembly and measurement of DHzFC and hydrazine-nitrate batteries.

The assembly of DHzFC is like OHzS, except that we use 20% Pt/C as the electrocatalyst of cathode ORR, and the catholyte is O<sub>2</sub>-saturated 1.0 M KOH. In hydrazine-nitrate batteries, the electrocatalyst of cathode and anode is Ru/CoP, but the catholyte is changed to 1.0 M KOH+0.3 M KNO<sub>3</sub>.

### 3.3 Calculation of electricity expense.

The electricity expense of electrocatalyst was calculated as follows:

$$W = (n \times U \times F) / 3.6 \times 10^6 \times V_m \times 10^{-3}$$

where  $W$  represents electricity expense when produced 1 m<sup>3</sup> H<sub>2</sub>. Moreover,  $n$ ,  $U$ , and  $V_m$  is the number of transferred electrons, cell voltage, and molar volume of gas (24.5 L/mol, 25 °C, 101 kPa).<sup>4</sup>

### 3.4 K<sup>+</sup> concentration measurement.

Electrolysis was carried out at a potential of -0.1 V vs. RHE. After 30 s of electrolysis, the working electrode was quickly transferred to pure water, and the voltage application was stopped at this time. Shake the working electrode for 1 min to ensure the desorption of K<sup>+</sup> adequately, and then test the concentration of K<sup>+</sup> by ICP.

### 3.5 Detection of NH<sub>3</sub> and calculation of NH<sub>3</sub> yield.

The detection of NH<sub>3</sub> is the same as our previous work.<sup>5,6</sup> Specifically, 2 mL of electrolyte after electrolysis was added in the 1.0 M NaOH mixed solution containing salicylic acid and trisodium sodium citrate dehydrate (2 mL, 5 wt%), then 1 mL of sodium hypochlorite solution (0.05 M) and 0.2 mL of sodium nitroferricyanide dihydrate (1 wt%) was added in the above mixed solution in turn. After 2 hours, the solution was tested by UV-Vis absorption spectrum. The calculation of NH<sub>3</sub> yield was follows as:

$$\text{NH}_3 \text{ yield} = C_{\text{NH}_3} \times V / (t \times S)$$

where  $V$ ,  $t$ , and  $S$  represent the volume of electrolyte in cathode cavity, electrolysis time, and area of working electrode.

### 3.6 N<sub>2</sub>H<sub>4</sub> adsorption measurement

In a solution of 1.0 M KOH + 0.1 M N<sub>2</sub>H<sub>4</sub>, the electrocatalyst was subjected to electrolysis for 100 s at different voltages (open-circuit potential, 0, and 0.1 V vs. RHE). Subsequently, 10 μL of the electrolyte adhering to the working electrode was promptly collected. After dilution, the electrolyte was treated with a chromogenic reagent to develop color, which was then used for UV-Vis absorption spectroscopy detection. The preparation of the chromogenic reagent refers to our previous work.<sup>5,6</sup>

#### 4. Finite element analysis (FEA).

The FEA was simulated by COMSOL Multiphysics, and the sample size was obtained by TEM.<sup>7</sup> The "Electric currents" and "electrostatics" modules are used to check the electric field of the electrode under a specific potential bias. The calculation formula of electric field is as follows:

$$E = -\nabla V$$

And the dielectric model is calculated as follows:

$$D = \varepsilon_0 \varepsilon_r V$$

where  $\varepsilon_0$  and  $\varepsilon_r$  is the dielectric constant of vacuum and materials.

In addition, by taking the light absorption and the generated volume power intensity as the input of temperature simulation, we studied the photothermal effect under the irradiation of 808 nm laser. The heat transfer equation is as follows:

$$\rho C_p \frac{\delta T(x,t)}{\delta t} + \rho C_p u \times \nabla T(x,t) = \nabla \cdot (k \nabla T(x,t)) + Q_1$$

where  $\rho$ ,  $C_p$ ,  $T(x,t)$ , and  $t$  represent density, heat capacity, local temperature, and time. Moreover,  $k$  and  $Q_1$  are thermal conductivity and thermal energy produced by photothermal effect.

#### 5. Theoretical calculation.

Vienna ab initio simulation software package (VASP) was carried out to conduct DFT calculations. Perdew Burke Ernzerhof (PBE) was used to simulate electron exchange-correlation energy. The cut-off energy of plane wave expansion is 400 eV, and the total energy convergence standard of is 10<sup>-5</sup>eV. All models applied a 15 Å vacuum layer on the z axis, the k-point grid of CoP and Ru/CoP is set to 2×2×1 (6). Gibbs free energy calculated follows the rule:

$$\Delta G = \Delta E_{\text{ads}} - \Delta ZPE - T\Delta S$$

where  $\Delta S$  and  $\Delta ZPE$  are the entropy and zero-point energy changes of the reaction at 298.15 K. When considering the influence of electric field on electrocatalyst, we applied electric field with -0.2 V•Å<sup>-1</sup> along the z axis.

#### 6. Calculation of techno-economic analysis (TEA).

In this work, assuming that the daily output of H<sub>2</sub> in the factory is 10 tons, the factory runs 21.6 hours a day (capacity coefficient is 0.9) and the Faraday efficiency in OHzS and OWS systems is 100%. Some other parameters are as follows: The cost of electrolyzer is \$300 USD/kWh, and the cost of catalyst and membrane accounts for 8% of the cost of electrolyzer, and its service life is 5 years. A rough cost calculation contains electrolyzer cost, electricity cost, other operating cost, balance of plant, and installation cost. The specific calculation was as follows:

$$\text{Electrolyzer cost} = \frac{\text{Capital recovery factor} \times \text{Total electrolyzer cost}}{\text{Capacity factor} \times 365 \times \text{Plant capacity}}$$

$$\text{Capital recovery factor (CRF)} = \frac{\text{Discount rate} \times (1 + \text{Discount rate})^{\text{lifetime}}}{(1 + \text{Discount rate})^{\text{lifetime}} - 1}$$

$$\text{Total electrolyzer cost} = \frac{\text{Power consumed} \times \text{base current density}}{\text{input current density}}$$

$$\text{Power consumed} = \text{Total current needed} \times \text{cell voltage}$$

$$\text{Total current needed} = \frac{\text{Plant capacity} \times \text{electrons transferred} \times \text{Faradaic constant}}{\text{Faradic efficiency}}$$

where discount rate is 7%.

$$\text{Electricity costs} = \frac{\text{Power consumed} \times \text{Electricity price} \times 24}{\text{Plant capacity}}$$

where electricity price is \$0.03 USD/kWh

$$\text{Other operating cost} = \text{Electricity cost} \times 15\%$$

we assume that other operating costs accounts for 15% of electricity cost

$$\text{Balance of plant} = \text{Balance of plant factor} \times \text{Capital cost}$$

where Balance of plant factor is 50%.

$$\text{Installation cost} = \text{Lang factor} \times \text{Capital cost}$$

where Lang factor is 1.

The price of water to be \$0.56 per ton, the price of KOH is \$872.1 per ton, and the price of hydrazine is \$2260 per ton. In terms of raw material costs, we focus on the production of H<sub>2</sub> under ideal conditions, while excluding recycling by-products other than H<sub>2</sub> (eg. H<sub>2</sub>O, N<sub>2</sub> and OH<sup>-</sup>). According to the electrochemical reaction equation, in the OHzS system, for every 1 mol of H<sub>2</sub> generated at the cathode, 2 electrons are transferred and 2 mol of H<sub>2</sub>O is consumed. Correspondingly, 0.5 mol of hydrazine is consumed at the anode. Based on this, we calculate the H<sub>2</sub>O consumed when produced 1 ton of H<sub>2</sub> through the following formula (The concentration of hydrazine in the anolyte of our OHzS system is 0.3 M):

$$\text{OWS: H}_2\text{O} = 1 \times \frac{18}{2} \times 2 + 1 \times \frac{18}{2} \times 2 = 36 \text{ ton}$$

$$\text{OHzS: H}_2\text{O} = \frac{32}{18} \times \frac{1}{0.3} + 1 \times \frac{18}{2} \times 2 = 23.92 \text{ ton}$$

The corresponding consumption of KOH is as follows:

$$\text{OWS: KOH} = 36 \times 1 \times 56.11 \div 1000 = 2.02 \text{ ton}$$

$$\text{OHzS: KOH} = 23.92 \times 1 \times 56.11 \div 1000 = 1.34 \text{ ton}$$

The hydrazine consumed corresponds to the anode:

$$\text{N}_2\text{H}_4 \text{ required} = 1 \times \frac{32}{2} \times 0.5 = 8 \text{ ton}$$

The cost of H<sub>2</sub>O is calculated as follows:

$$\text{Cost of H}_2\text{O}_{\text{OHZS}} = 23.92 \times 0.56 = 13.4 \text{ \$/ton}$$

$$\text{Cost of H}_2\text{O}_{\text{OWS}} = 36 \times 0.56 = 20.16 \text{ \$/ton}$$

The cost of KOH is calculated as follows:

$$\text{Cost of KOH}_{\text{OWS}} = 2.02 \times 872.1 = 1761.64 \text{ \$/ton}$$

$$\text{Cost of KOH}_{\text{OHZS}} = 1.34 \times 872.1 = 1168.61 \text{ \$/ton}$$

The cost of N<sub>2</sub>H<sub>4</sub> is calculated as follows:

$$\text{Cost of N}_2\text{H}_4 = 8 \times 2260 = 18080 \text{ \$/ton}$$

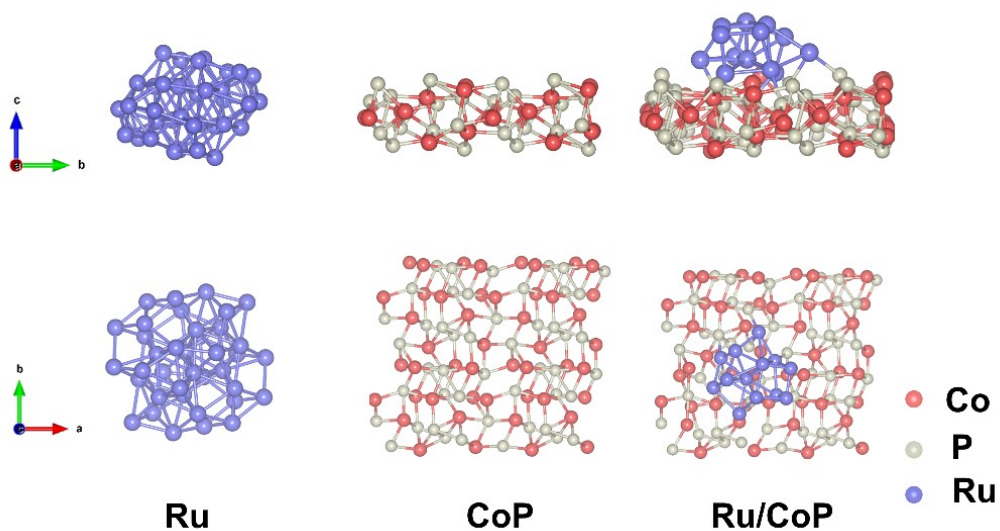


**Fig. S1.** The models of Ru, CoP, and Ru/CoP.

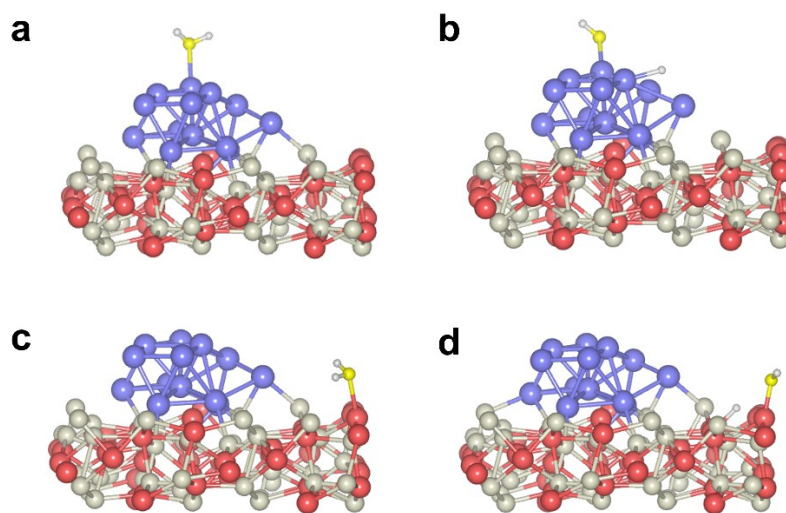


**Fig. S2.** The models of H<sub>2</sub>O adsorption (a, c) and H<sub>2</sub>O dissociation (b, d) at Ru site and Co site.

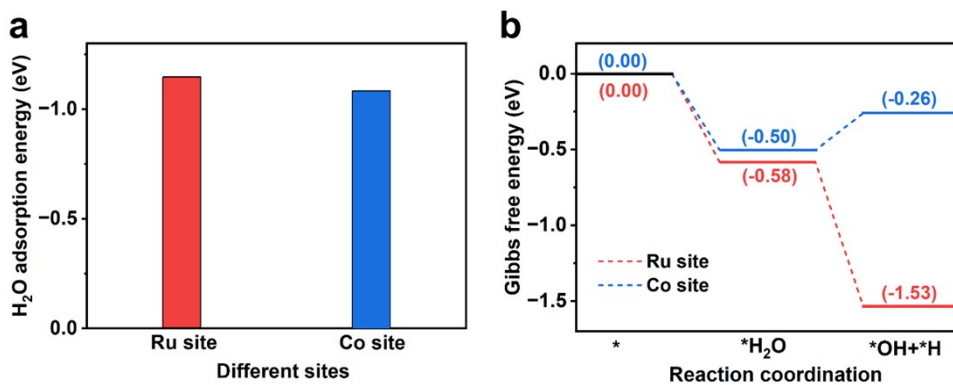


**Fig. S3.** (a) H<sub>2</sub>O adsorption energy and (b) Gibbs free energy for H<sub>2</sub>O adsorption and dissociation at different sites on Ru/CoP.

As shown in Fig. S3, the adsorption and dissociation of H<sub>2</sub>O tend to occur at the Ru site on Ru/CoP rather than that of Co site. Therefore, we only investigate the adsorption and dissociation of H<sub>2</sub>O on Ru site when the electric field is applied.

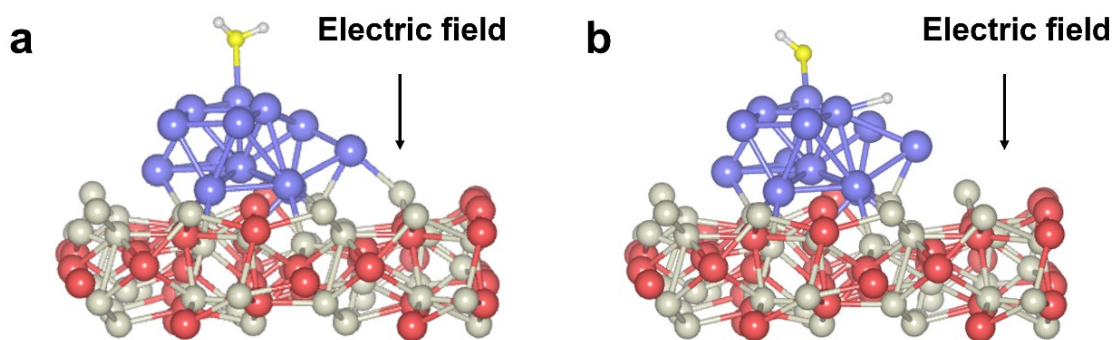


**Fig. S4.** The models of (a) H<sub>2</sub>O adsorption and (b) H<sub>2</sub>O dissociation on Ru/CoP under extra electric field.

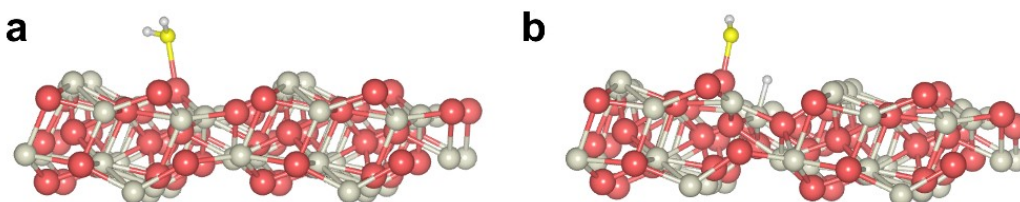


**Fig. S5.** The models of (a) H<sub>2</sub>O adsorption and (b) H<sub>2</sub>O dissociation on CoP.

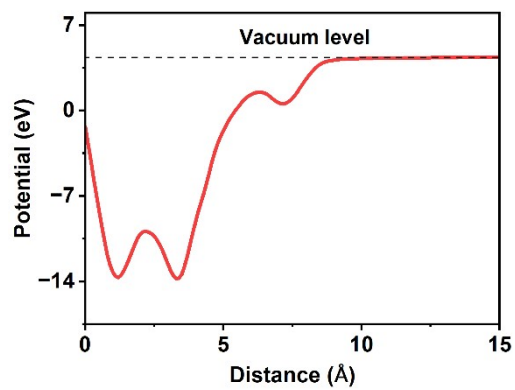


Fig. S6. Work function of Ru/CoP.

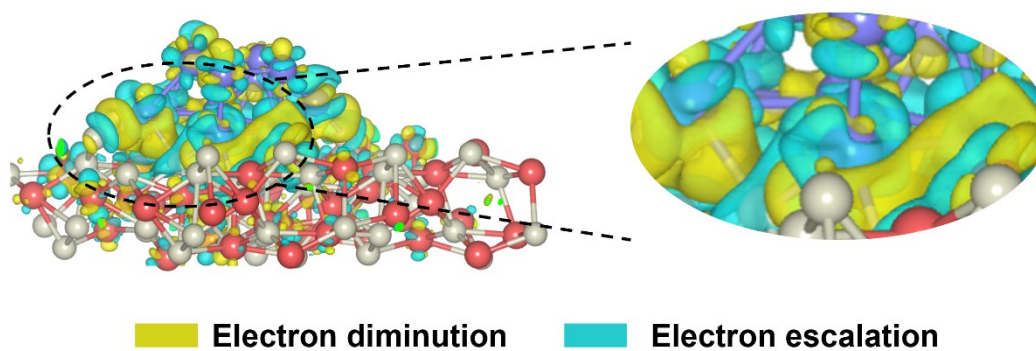


Fig. S7. Charge density difference of Ru/CoP.

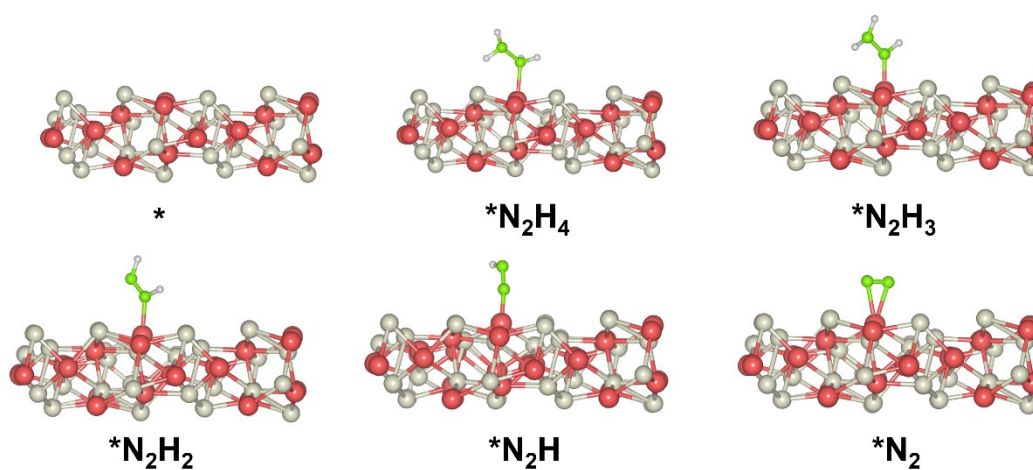
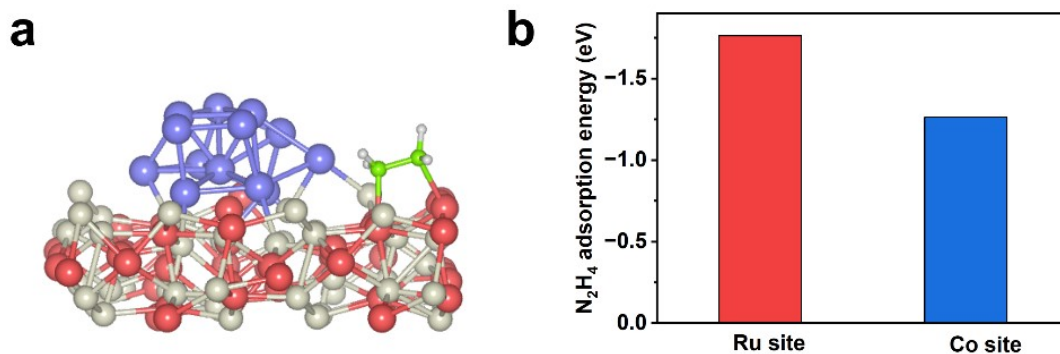
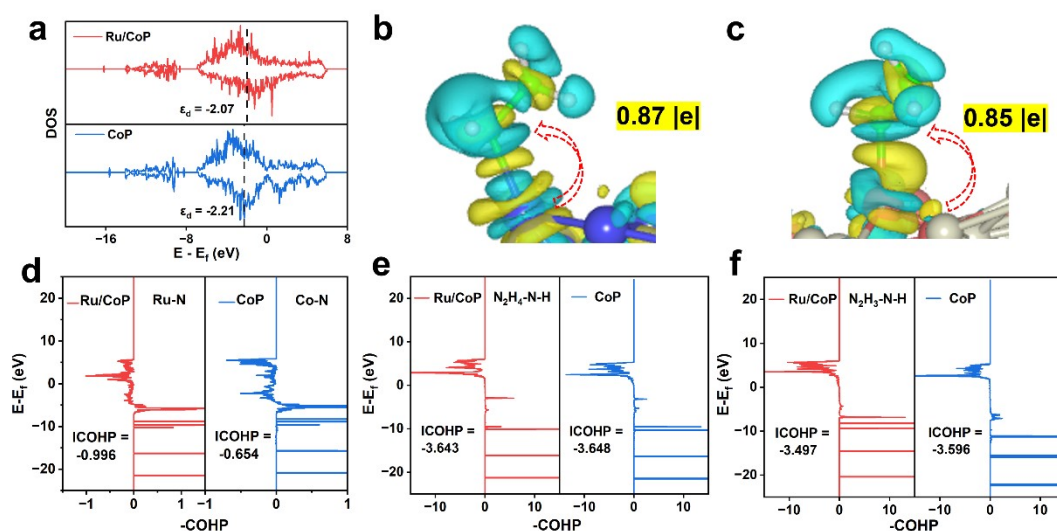


Fig. S8. The models of CoP for HzOR.



**Fig. S9.** (a) The model of  $\text{N}_2\text{H}_4$  adsorbed on Ru/CoP. (b)  $\text{N}_2\text{H}_4$  adsorption energy at Ru and Co site on Ru/CoP.

As shown in Fig. S9b, Ru site exhibits a more negative  $\text{N}_2\text{H}_4$  adsorption energy compared to Co site, indicating that  $\text{N}_2\text{H}_4$  tends to adsorb on Ru site rather than Co site in Ru/CoP.



**Fig. S10.** (a) DOS of Ru/CoP and CoP. The charge density difference and Bader charge analysis of  $^*\text{N}_2\text{H}_4$  on (b) Ru/CoP and (c) CoP. (d) COHP of Ru-N and Co-N. COHP of N-H for Ru/CoP and CoP in (e)  $\text{N}_2\text{H}_4$  and (f)  $\text{N}_2\text{H}_3$ .

As shown in Fig. S10a, the d-band center of Ru/CoP shifts upwards compared to CoP, suggesting better  $\text{N}_2\text{H}_4$  adsorption on Ru/CoP. Bader charge analysis shows more electron transfer from the electrocatalyst to the N atom in the  $^*\text{N}_2\text{H}_4$  intermediate for Ru/CoP than CoP, indicating a stronger interaction beneficial for adsorption (Figs. S10b and S10c). As shown in Fig. S10d, the result of Integrated crystal orbital Hamilton population (ICOHP) of Ru-N and Co-N bonds reveals a stronger Ru-N interaction (a more negative ICOHP value (larger absolute value) indicates a stronger bonding interaction between atoms).<sup>8,9</sup> These results show that the built-in electric field raises the d-band center, promotes electron transfer, and enhances  $\text{N}_2\text{H}_4$  adsorption. As shown in Figs. S10e and S10f, the COHP of N-H bonds in  $^*\text{N}_2\text{H}_4$  and  $^*\text{N}_2\text{H}_3$  intermediates (rate-determining steps in CoP and Ru/CoP) were calculated. The lower ICOHP of N-H bonds on Ru/CoP implies more electron occupancy in antibonding orbitals, facilitating dehydrogenation in HzOR process.

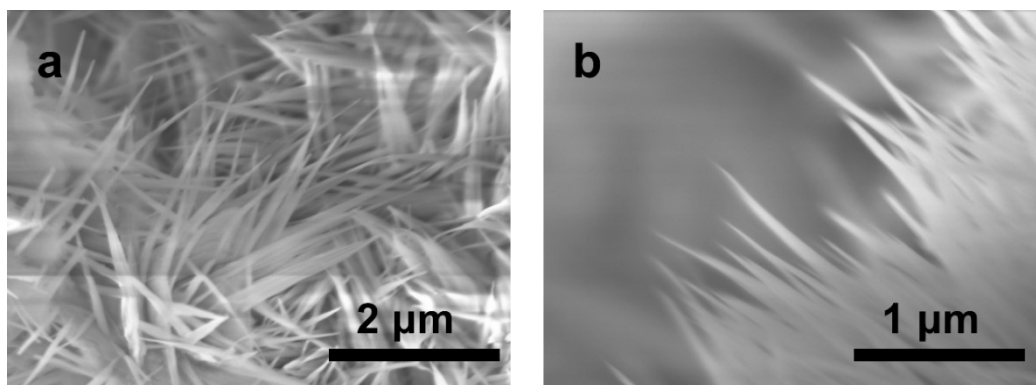


**Fig. S11.** (a, b) SEM image of Co(OH)F.

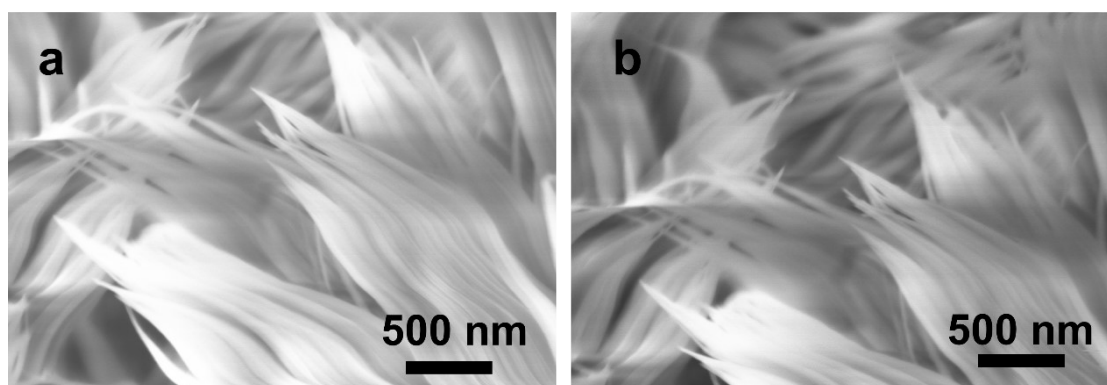


**Fig. S12.** (a, b) SEM image of bulk-like Co(OH)F (Co(OH)F-B).

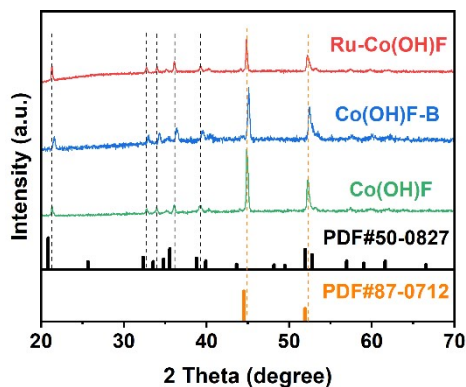


**Fig. S13.** XRD patterns of Co(OH)F, Co(OH)F-B, and Ru-Co(OH)F.

As shown in Fig. S13, the XRD patterns of Co(OH)F, Co(OH)F-B, and Ru-Co(OH)F are indexed to Co(OH)F (PDF#29-0497), with peaks at 45° and 52° corresponding to the Ni foam. No new peaks were observed in Ru-Co(OH)F, confirming that there is no new phase following ion exchange. Notably, due to the different heights of the samples during the XRD testing process, an overall shift occurred in the XRD peak positions.

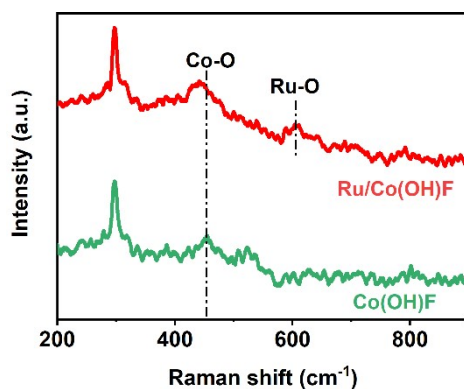


**Fig. S14.** Raman spectra of Co(OH)F and Ru-Co(OH)F.

As shown in Fig. S14, a peak at around 600  $\text{cm}^{-1}$  appeared in the Raman spectra in Ru-Co(OH)F, corresponding to the vibration of Ru-O. Meanwhile, the Co-O peak in Ru-Co(OH)F has blue-shifted compared to Co(OH)F. These results confirm the ions exchange between  $\text{Ru}^{3+}$  and  $\text{Co(OH)}_2$ .

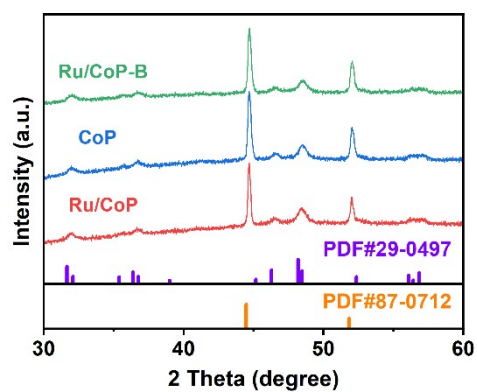


**Fig. S15.** XRD patterns of CoP and Ru/CoP.

As shown in Fig. S15, the XRD patterns of CoP and Ru/CoP are indexed to CoP (PDF#29-0497), which prove the successful synthesis of CoP and Ru/CoP.

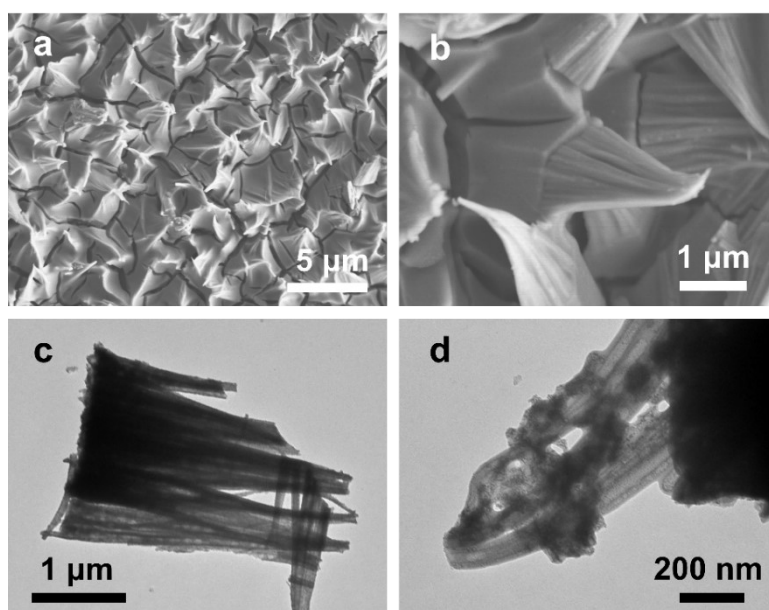


**Fig. S16.** (a, b) SEM images and (c, d) TEM images of Ru/CoP-B.

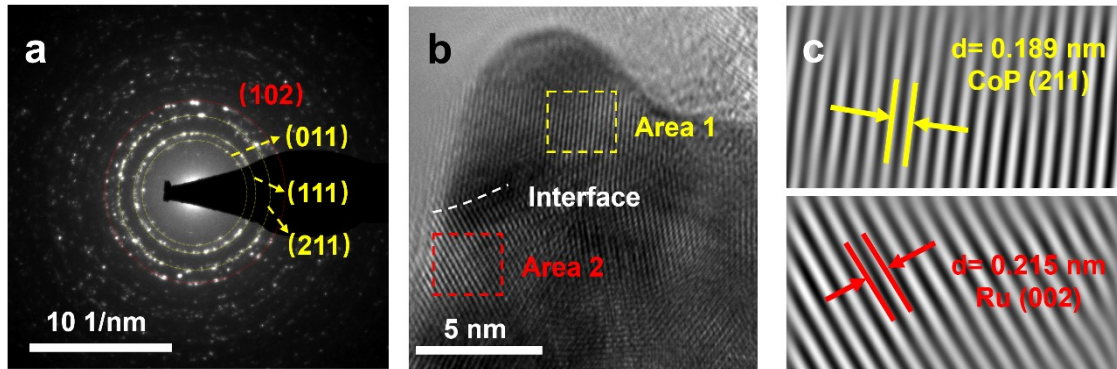


**Fig. S17.** (a) SAED patterns and (b) HRTEM image of Ru/CoP. (c) FFT image in Area 1 (top) and Area 2 (bottom).

As shown in Fig. S17a, the selected area electron diffraction (SAED) revealed a typical polycrystalline concentric ring pattern and planes corresponding to CoP and Ru, which confirmed the heterostructure. Then, analysis of the nanoparticles on the nanoneedles (Fig. S17b) showed a distinct interface between area 1 and area 2 corresponding to CoP (211) and Ru (002) planes, indicating the nanoparticles mainly consisted of CoP, Ru, and the interface between them.

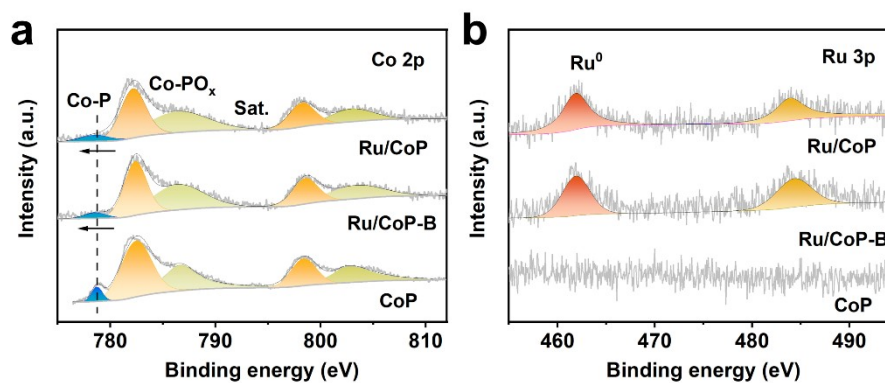


**Fig. S18.** (a) Co 2p and (b) Ru 3p XPS spectra of CoP, Ru/CoP, and Ru/CoP-B.

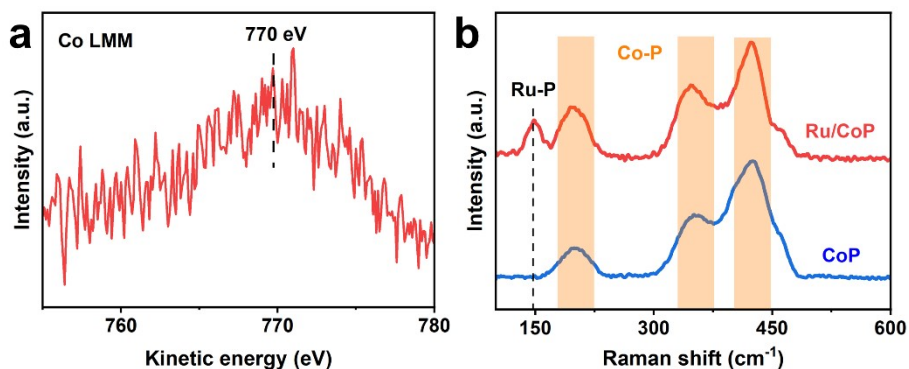


**Fig. S19.** (a) Co LMM spectrum of Ru/CoP. (b) Surface-enhanced Raman spectra of Ru/CoP and CoP.

As shown in Fig. S19, there is a distinct peak around 770 eV (kinetic energy), which corresponds to a state where Co<sup>2+</sup> and Co<sup>3+</sup> co-exist.<sup>10,11</sup> As shown in Fig. S19b, the peaks correspond to the Co-P bond in both CoP and Ru/CoP samples. Integrating XRD and HRTEM results indicate CoP presence in both. Notably, the Ru/CoP sample has an extra 147 cm<sup>-1</sup> Raman peak for the Ru-P bond.<sup>12</sup> XPS showed that Ru existed in Ru/CoP in the form of metallic Ru, which indicated that Ru nanoparticles in Ru/CoP combined with CoP instead of forming RuP<sub>2</sub>. These results suggest Ru nanoparticles interact with CoP through P atoms in Ru/CoP, validating our proposed model.

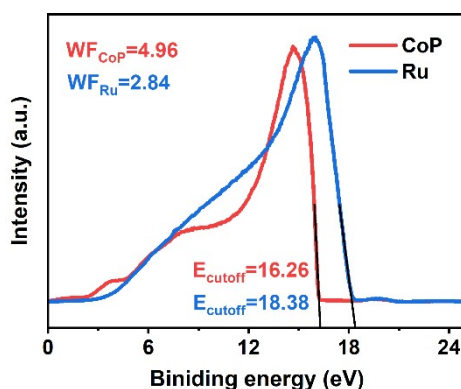


**Fig. S20.** UPS spectra of Ru and CoP.

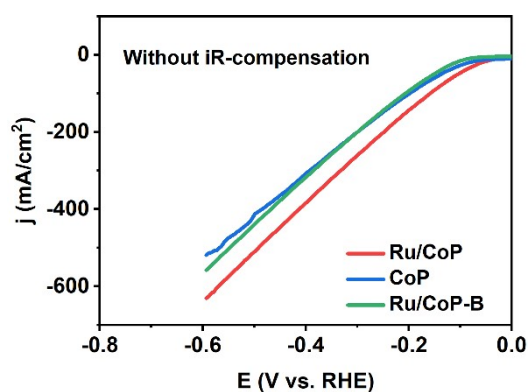


**Fig. S21.** LSV curves of Ru/CoP, CoP, and Ru/CoP-B without iR-compensation.

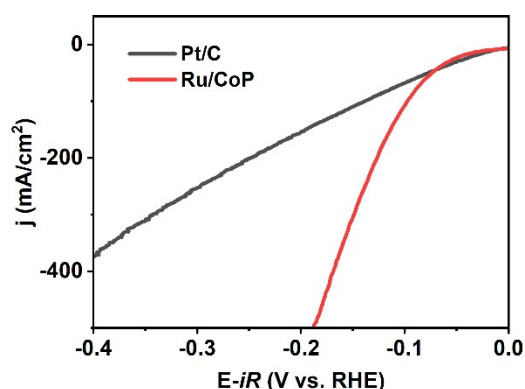


**Fig. S22.** LSV curves of Pt/C and Ru/CoP.

The Pt/C electrode was prepared by depositing an ink containing 20% Pt/C onto nickel foam. Specifically, 30 mg of Pt/C was dispersed in a mixed solution consisting of 950  $\mu\text{L}$  of isopropanol and 50  $\mu\text{L}$  of Nafion. After 30 minutes of ultrasonic treatment, 100  $\mu\text{L}$  of the electrocatalyst ink was uniformly deposited onto the nickel foam, with a specified dropping area of 1  $\text{cm}^2$ .

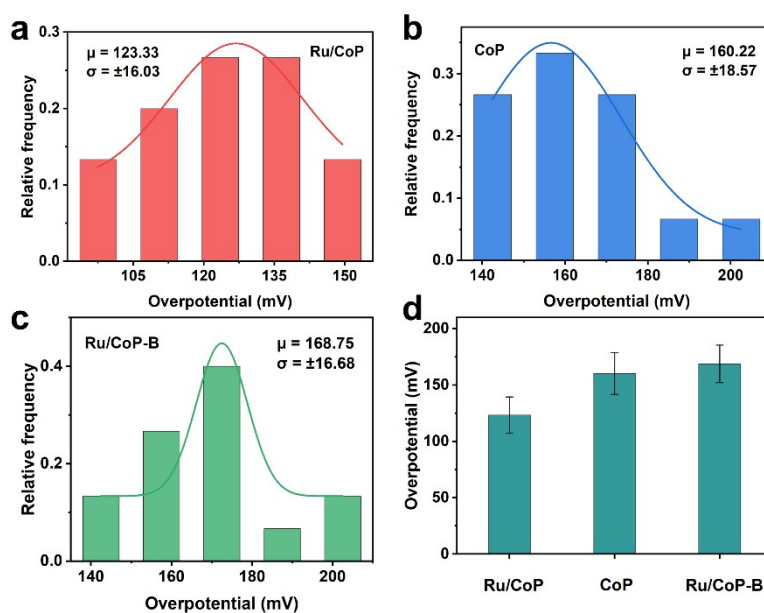


**Fig. S23.** Distribution of HER overpotential at the current density of 100  $\text{mA}/\text{cm}^2$  of (a) Ru/CoP, (b) CoP, and (c) Ru/CoP-B. (d) Average overpotential of Ru/CoP, CoP, and Ru/CoP-B at the current density of 100  $\text{mA}/\text{cm}^2$ .

As shown in Fig. S23, the average overpotential of Ru/CoP was 123.33 mV with a standard deviation of only  $\pm 16.03$  mV. For CoP, the average overpotential was 160.22 mV and the standard deviation was  $\pm 18.57$  mV. For Ru/CoP-B, the average overpotential was 168.75 mV and the standard deviation was  $\pm 16.68$  mV. The small deviations of these three groups of samples indicate the high stability and reproducibility of the HER activity of the synthesized samples.

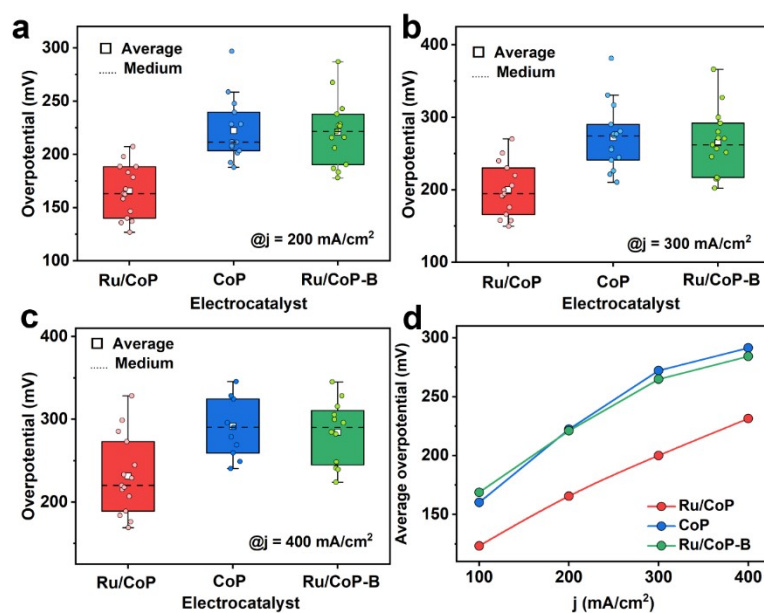


**Fig. S24.** Overpotential at the current density of (a) 200, (b) 300, and (c) 400 mA/cm<sup>2</sup>. (d) Average overpotential at different current densities of Ru/CoP, CoP, and Ru/CoP-B.

As shown in Fig. S24, Ru/CoP exhibits the best HER activity across all current densities. Notably, the activity of CoP is higher than that of Ru/CoP-B at lower current densities, however, the activity of CoP gradually falls below that of Ru/CoP-B as the current density increases. Since a large amount of \*H needs to be dimerized to form H<sub>2</sub> at higher current densities, we speculate that the observed change in activity is primarily due to the insufficient hydrolytic dissociation ability of CoP at elevated current densities, which influences \*H from being supplied in a timely manner.

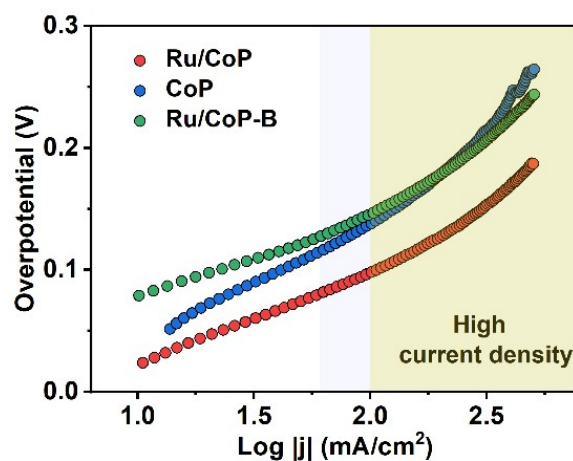


**Fig. S25.** Tafel slope of Ru/CoP, CoP, and Ru/CoP-B.

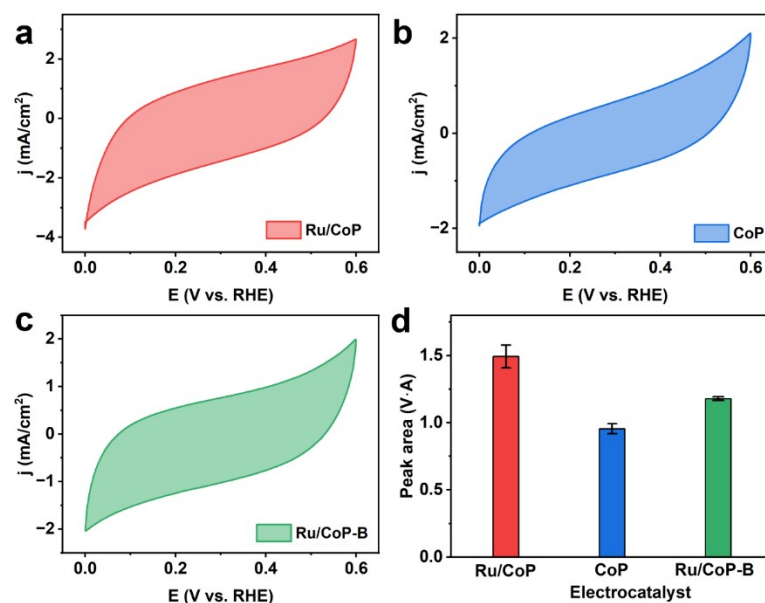


**Fig. S26.** CV curves of (a) Ru/CoP, (b) CoP, and (c) Ru/CoP-B. (d) CV peak area of Ru/CoP, CoP, and Ru/CoP-B.

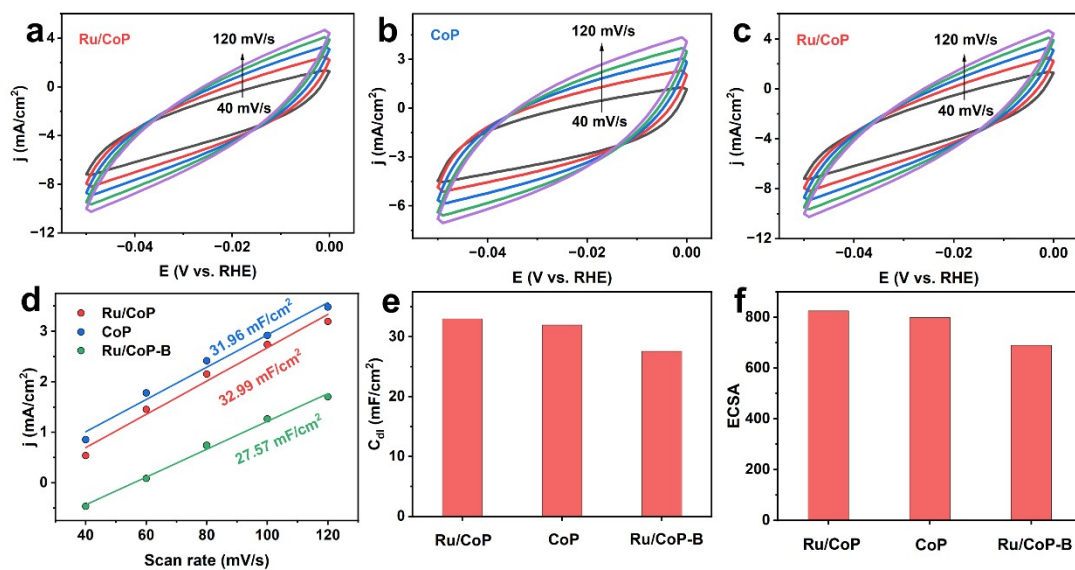


**Fig. S27.** CV curves of (a) Ru/CoP, (b) CoP, and (c) Ru/CoP-B. (d)  $C_{dl}$  values of Ru/CoP, CoP, and Ru/CoP-B. Comparison of (e)  $C_{dl}$  values and (f) ECSA for Ru/CoP, CoP, and Ru/CoP-B.

As shown in Fig. S27, the values of  $C_{dl}$  and ECSA of Ru/CoP, CoP and Ru/CoP-B decrease in turn, confirming that the needle-like structure facilitates the exposure of a greater number of active sites.

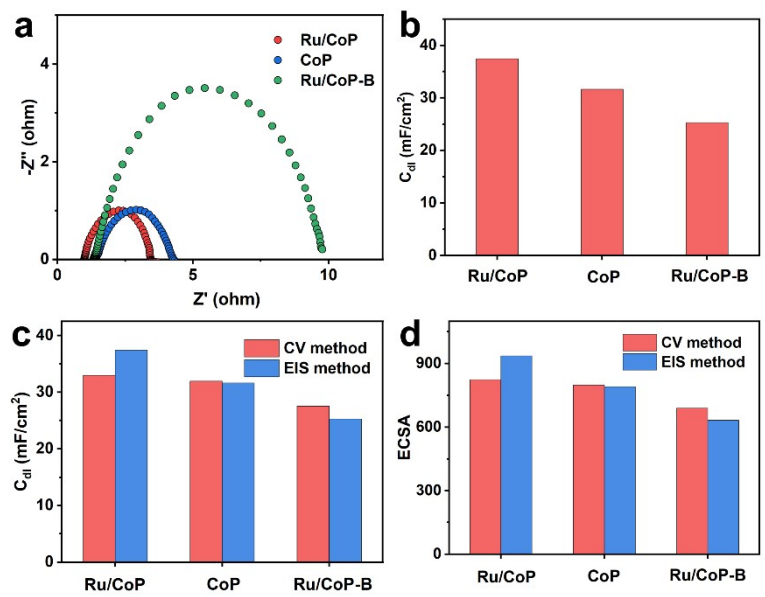


**Fig. S28.** (a) EIS plots and (b) Comparison of  $C_{dl}$  values for Ru/CoP, CoP, and Ru/CoP-B. Comparison of (c)  $C_{dl}$  value and (d) ECSA calculated by CV and EIS methods.

As shown in the Fig. S28c and S28d, there is a small difference between the  $C_{dl}$ /ECSA value calculated by fitting EIS plots and the result calculated by CV curves, which shows the accuracy of ECSA.

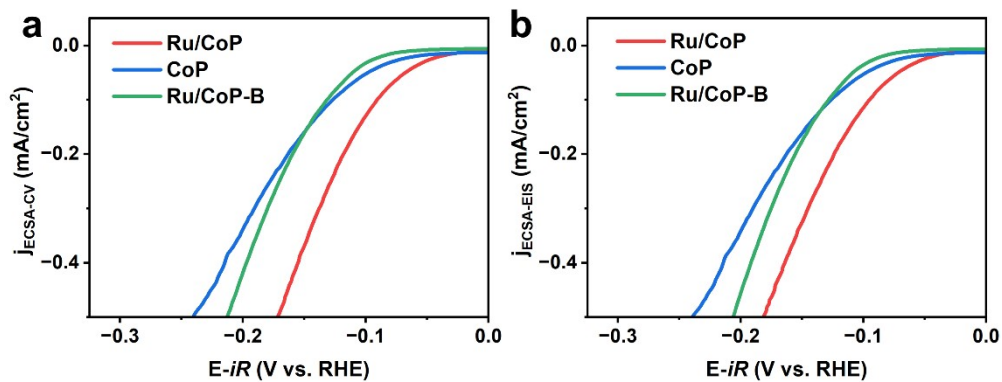


**Fig. S29.** LSV curves normalized by ECSA calculated by (a) CV method and (b) EIS method.

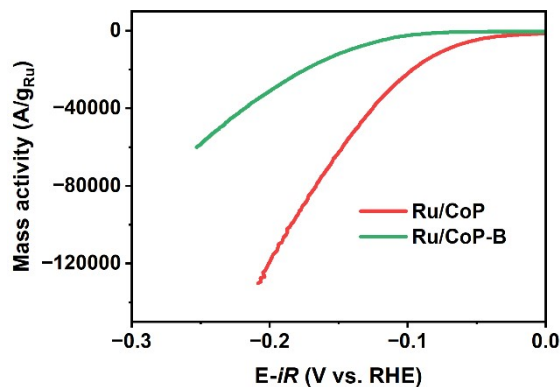


Fig. S30. Mass activity of Ru/CoP and Ru/CoP-B for HER.

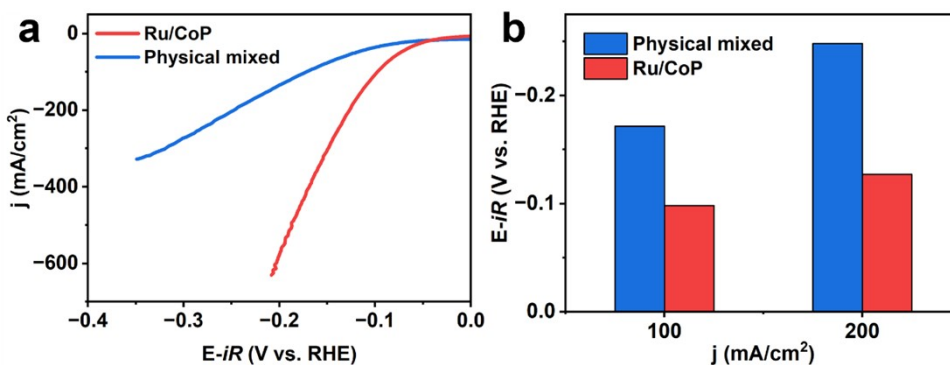


Fig. S31. LSV curves of Ru/CoP and the physical mixed Ru-CoP.

Physical mixed Ru-Cu is prepared by uniformly dropping commercial Ru/C ink on CoP, and the specific method is like the preparation of Pt/C electrode.

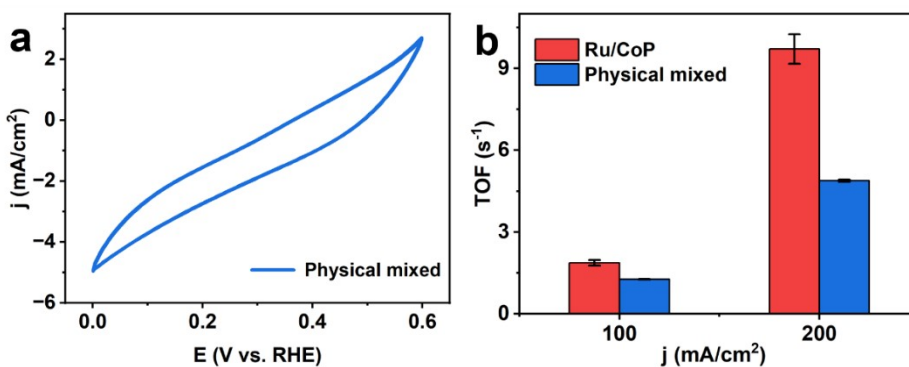
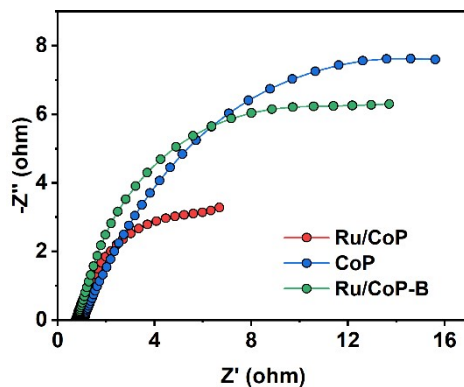
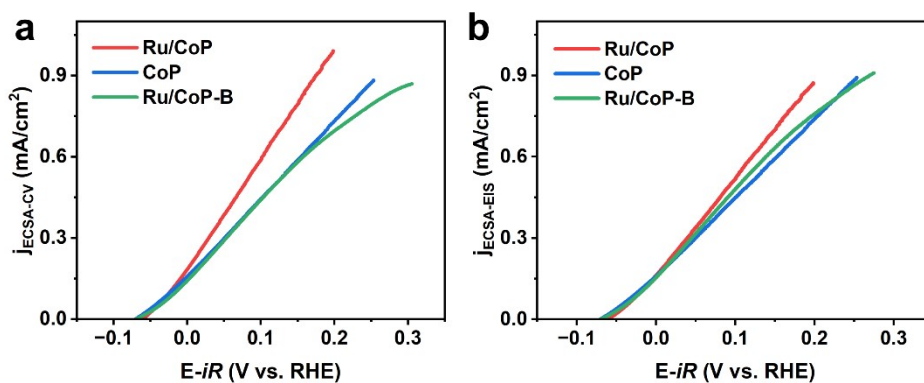


Fig. S32. (a) CV curve of physical mixed Ru/CoP. (b) TOF values at the current density of 100 and 200 mA/cm<sup>2</sup> of Ru/CoP and the physical mixed electrocatalyst.



**Fig. S33.** EIS plots of Ru/CoP, CoP, and Ru/CoP-B.

As shown in Fig. S33, Ru/CoP shows the smallest semicircle, indicating its rapid charge transfer.



**Fig. S34.** LSV curves normalized by ECSA calculated by (a) CV method and (b) EIS method.

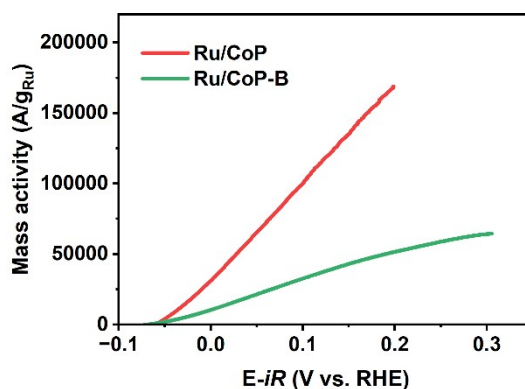


**Fig. S35.** Mass activity of Ru/CoP and Ru/CoP-B for HzOR.

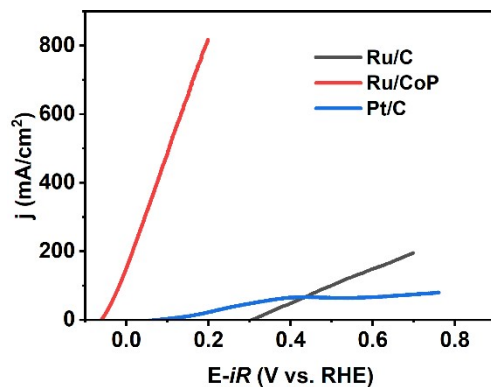


**Fig. S36.** LSV curves of Ru/C, Pt/C, and Ru/CoP.

The preparation of Ru/C electrode is like that of Pt/C except that Ru/C replaces Pt/C. Interestingly, both Ru/C and Pt/C and Ru/C show poor HzOR activity, so it is more important to develop high-performance HzOR electrocatalysts.

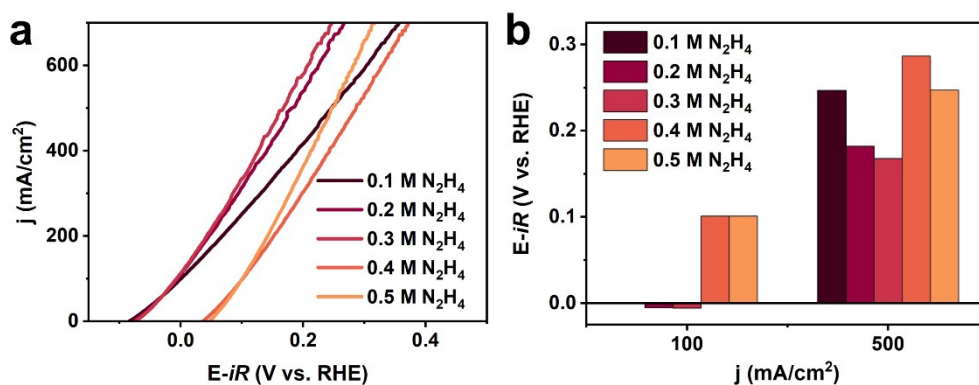


**Fig. S37.** (a) LSV curves and (b) Potential at the current density of 100 and 500 mA/cm<sup>2</sup> of Ru/CoP in 1.0 M KOH with different content of N<sub>2</sub>H<sub>4</sub>.

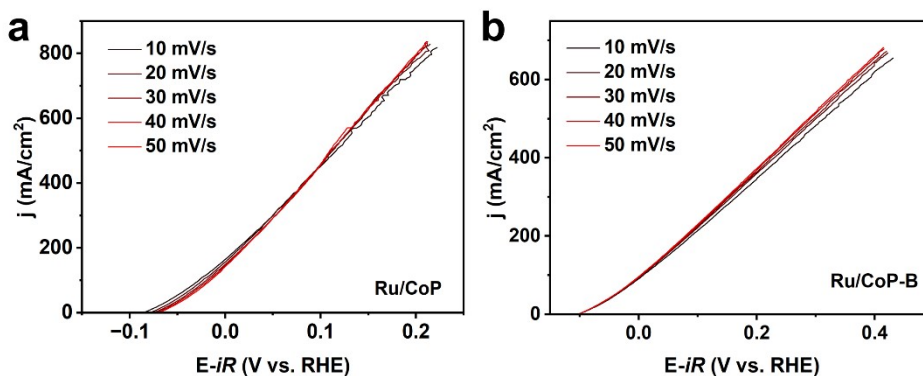


**Fig. S38.** LSV curves with different scan rates of (a) Ru/CoP and (b) Ru/CoP-B.

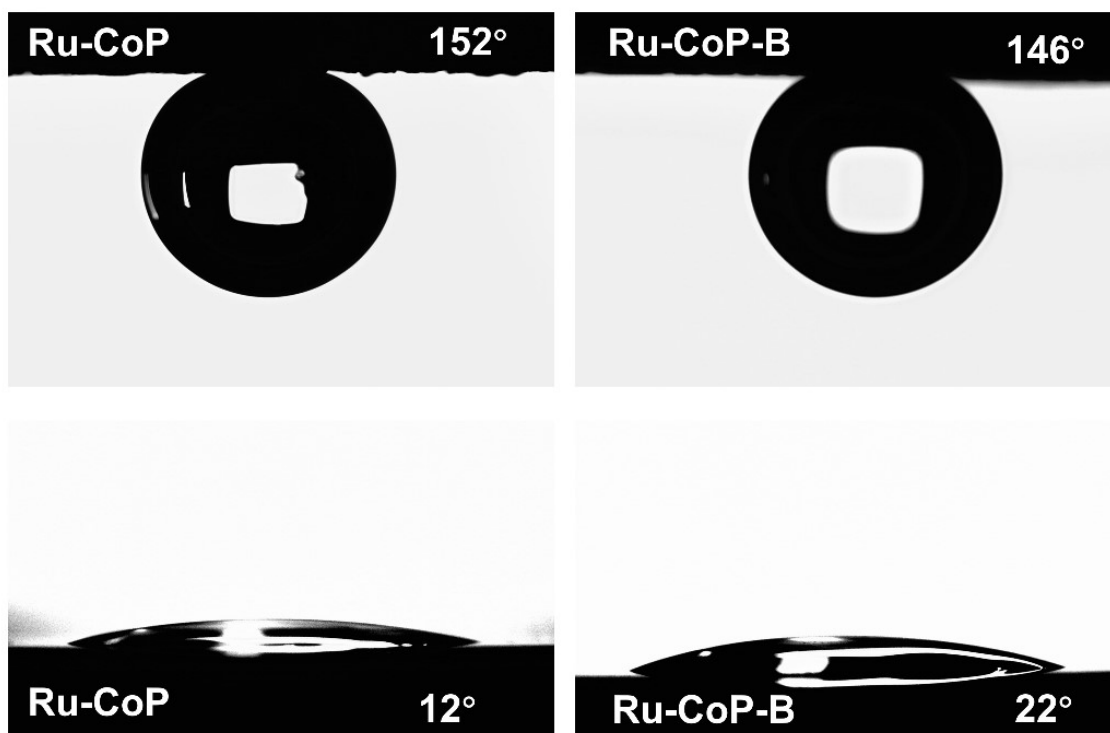


Fig. S39. The contact angle experiment of Ru/CoP and Ru/CoP-B.

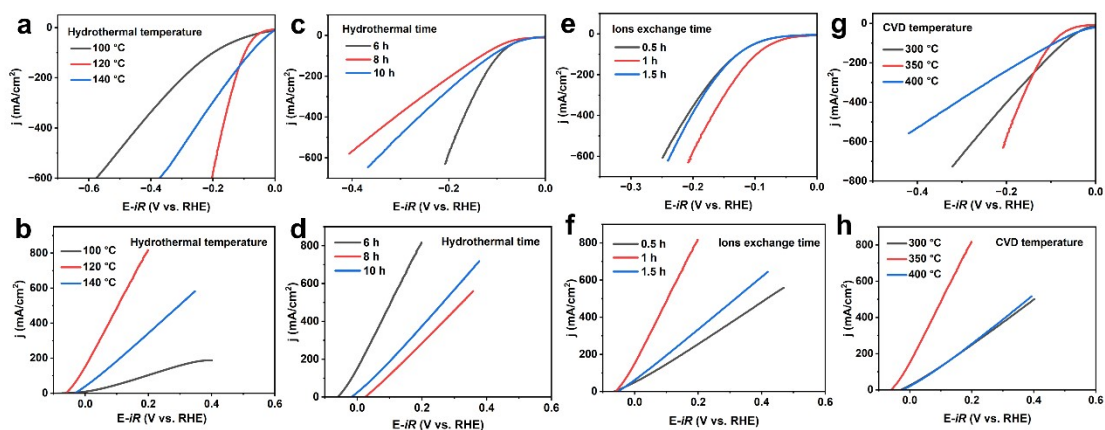
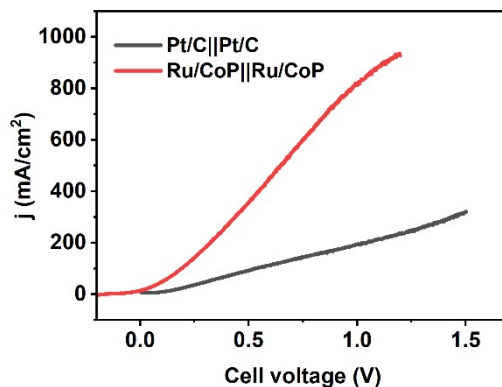
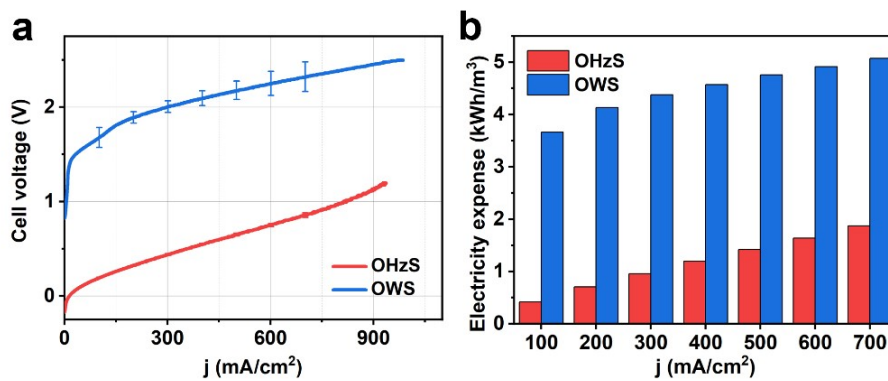


Fig. S40. Optimization of synthesis conditions of Ru/CoP, CoP and Ru/CoP-B. LSV curves for (a) HER and (b) HzOR at different hydrothermal temperatures. LSV curves for (c) HER and (d) HzOR with different hydrothermal time. LSV curves for (e) HER and (f) HzOR with different ions exchange time. LSV curves for (g) HER and (h) HzOR at different chemical vapor deposition temperatures.



**Fig. S41.** LSV curves of OHzS system used Pt/C||Pt/C and Ru/CoP||Ru/CoP as anode and cathode. As shown in Fig. S41, although Pt/C has excellent HER activity, its HzOR activity is poor (Fig. S27), which may be the reason for the poor performance of OHzS system with Pt/C as anode and cathode.



**Fig. S42.** (a) LSV curves of OHzS and OWS system. (b) Electricity expense at different current density of OHzS and OWS system.

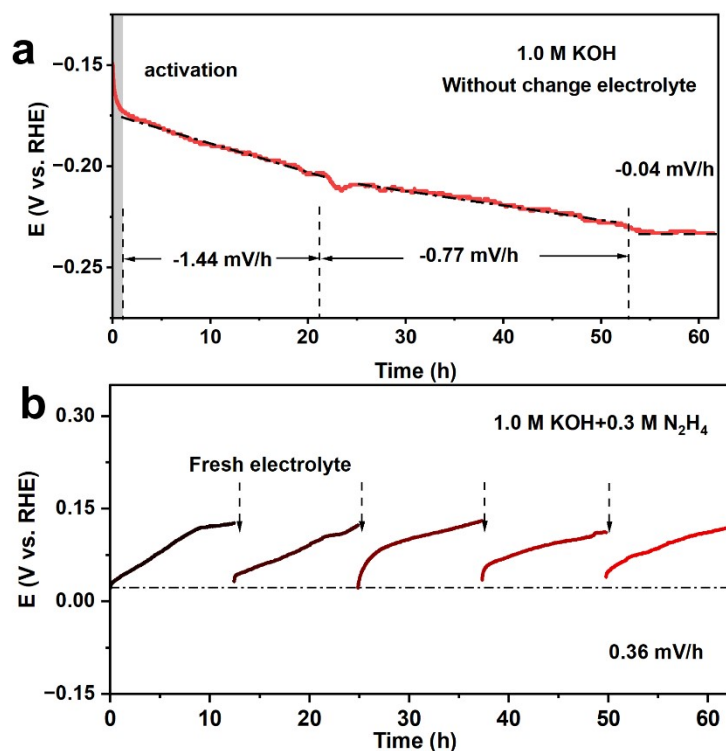


**Fig. S43.** Stability of Ru/CoP for (a) HER and (b) HzOR in three-electrode system.

To explore the cause of early-stage activity decline in the OH<sub>2</sub>S system stability, we carried out HER and HzOR stability tests in a three-electrode system at 100 mA/cm<sup>2</sup>. The HER activity changed notably within the first 60 h. By calculating the slope of the potential change over time, its activity change was divided into stages: a sharp drop in the initial 2 h related to electrocatalyst activation, a relatively fast decrease from the 2nd to 22nd h (-1.44 mV/h), a gradual slowdown after the 22nd h (-0.77 mV/h), and near-stability after the 52nd h (-0.04 mV/h). For HzOR stability testing, due to electrolyte replacement and workstation limitations, we cycled the sample 5 times (each cycle lasted 12.5 h, and the conditions remained the same for each cycle, including electrocatalyst, electrolyte volume and concentration). The potential rose in each cycle, but activity mostly recovered after electrolyte replacement, suggesting little activity loss during HzOR. In summary, the initial decline in OH<sub>2</sub>S system stability is mainly due to the decrease in HER activity.

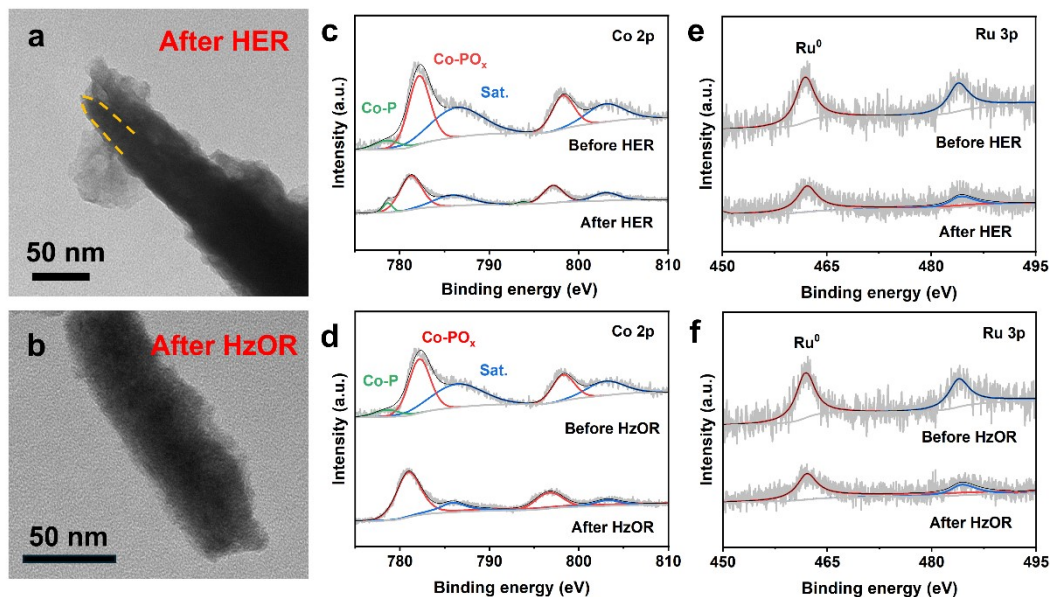


**Fig. S44.** TEM images of Ru/CoP after (a) HER and (b) HzOR. Co 2p XPS spectra before and after (c) HER and (d) HzOR. Ru 3p XPS spectra before and after (e) HER and (f) HzOR.

As shown in Figs. S44a and S44b, the needle-like structure remains after HER stability, but the needle-like structure gradually collapses into a rod-like structure after HzOR. As demonstrated in Figs. S44c and S44d, the Co 2p XPS spectra revealed that the Co-P bond persisted after the HER stability test but disappeared after the HzOR stability test, mainly due to Co-P oxidation. It has been reported that the oxidation of the Co-P bond can be restored during the HzOR process. Notably, the peak intensity of Co 2p decreased after the HER stability test. We hypothesize that this might be due to Co dissolution. To confirm this, we conducted an ICP test on the electrolyte after the HER stability test. The results showed that the Co content in the electrolyte was about 0.85 ppm and the Ru content was about 0.042 ppm. Furthermore, XPS tests on the post-test samples indicated that the Ru 3p peaks remained essentially unchanged after both HER and HzOR stability tests (Figs. S44e and S44f).

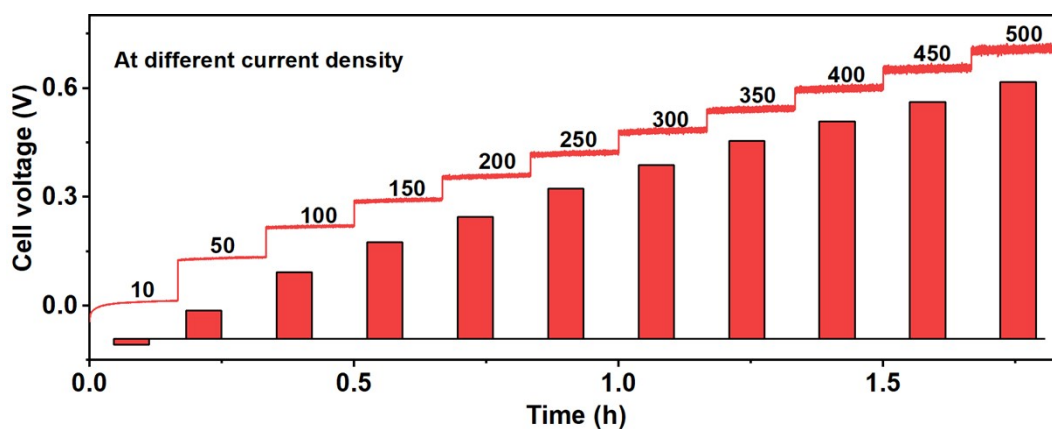


**Fig. S45.** Cell voltage at different current density of OHZS system.

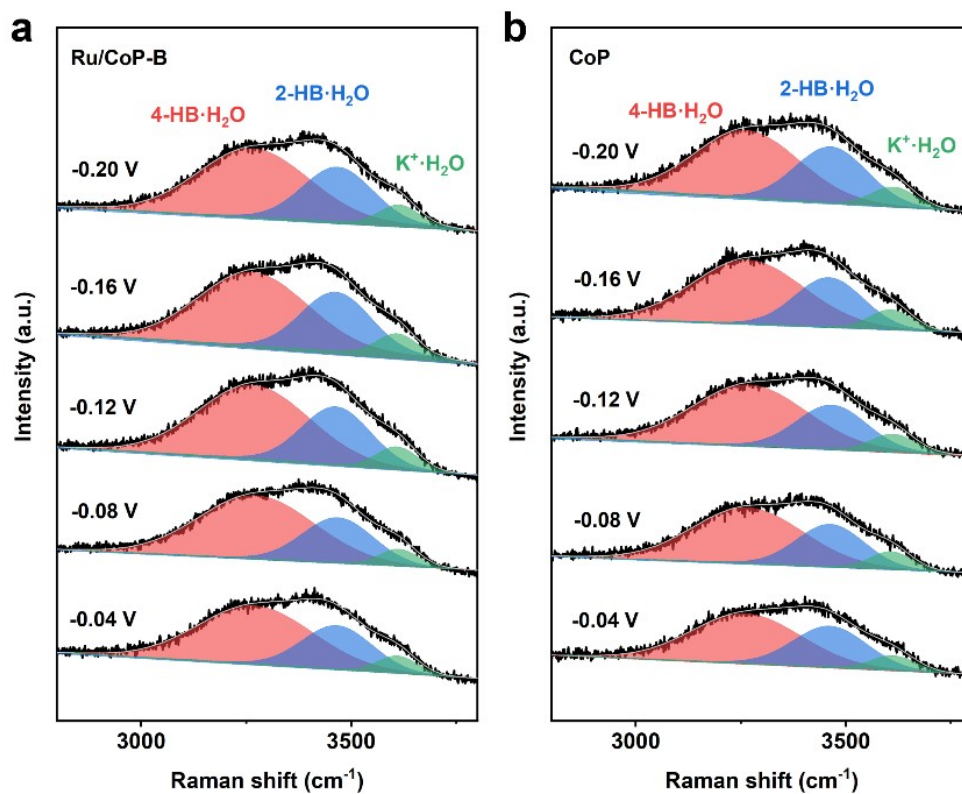


Fig. S46. In-situ Raman spectra of (a) Ru/CoP-B and (b) CoP.

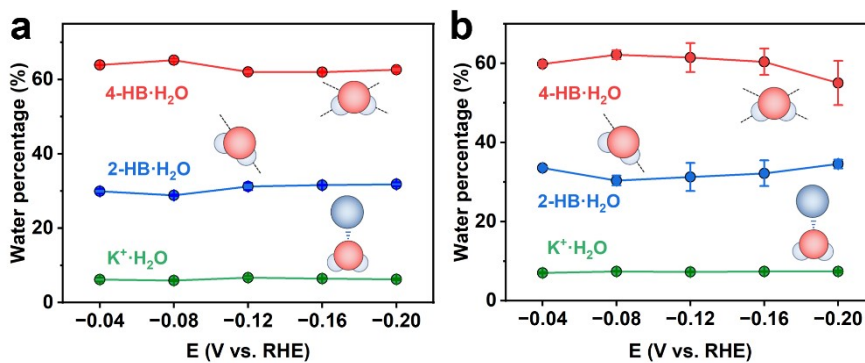


Fig. S47. Water percentage of (a) Ru/CoP-B and (b) CoP.

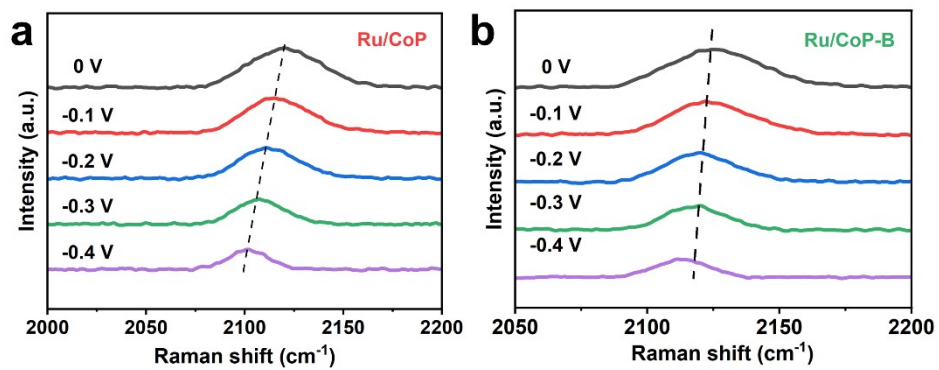


Fig. S48. In-situ SERS of (a) Ru/CoP and (b) Ru/CoP-B.

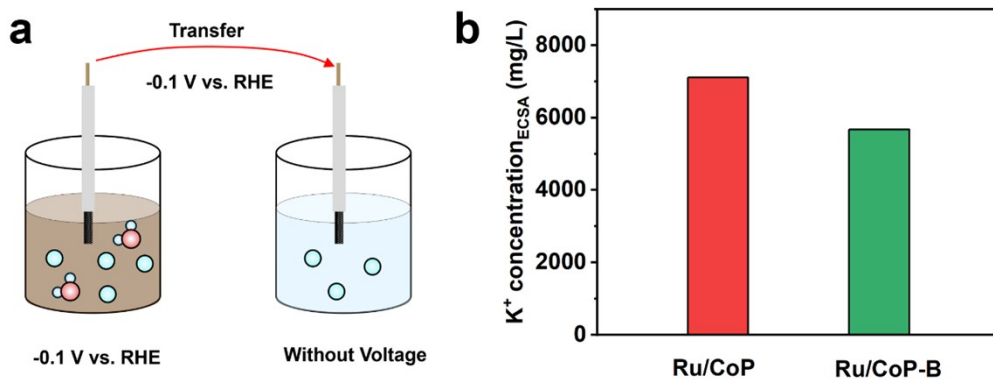
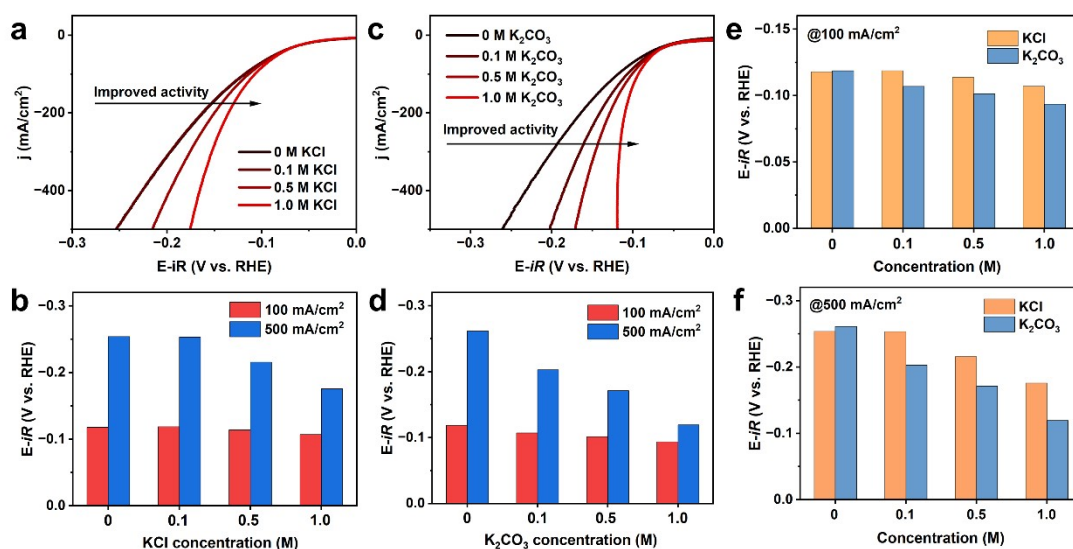
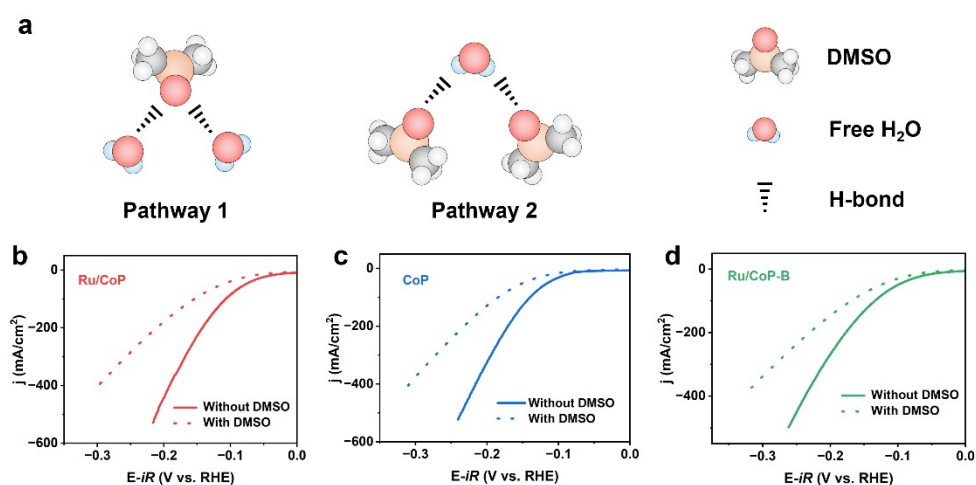


Fig. S49. (a) Schematic diagram of K<sup>+</sup> concentration test. (b) K<sup>+</sup> concentration normalized by ECSA of Ru/CoP and Ru/CoP-B.



**Fig. S50.** LSV curves in 1.0 M KOH with different concentration of (a) KCl and (b) K<sub>2</sub>CO<sub>3</sub>. (c) Current density at -0.1 and -0.5 V in 1.0 M KOH with different concentration of K<sub>2</sub>CO<sub>3</sub>. (d) Potential at 500 mA/cm<sup>2</sup> in 1.0 M KOH with different concentration of KCl and K<sub>2</sub>CO<sub>3</sub>.

As shown in Fig. S50c, HER activity was also enhanced with the increase in K<sub>2</sub>CO<sub>3</sub> concentration. Due to the stoichiometric ratio, the activity increased by adding K<sub>2</sub>CO<sub>3</sub> is higher than that of KCl with the same molar number (Figs. S50e and 50f). This not only demonstrates the positive effect of K<sup>+</sup> on the activity of HER, but also that this enhancement in activity is independent of anions.



**Fig. S51.** (a) Schematic diagram of H-bond between DMSO and free H<sub>2</sub>O. LSV curves with and without DMSO of (b) Ru/CoP, (c) CoP, and (d) Ru/CoP-B.

Figure S51a illustrates two mechanisms by which DMSO can form H-bonds with free water. In comparison to 4-HB·H<sub>2</sub>O and 2-HB·H<sub>2</sub>O, free water (K<sup>+</sup>·H<sub>2</sub>O) is more readily dissociated. Consequently, the formation of this H-bond results in a reduction of free water and subsequently diminishes HER activity. The greater the decrease in HER activity following the addition of DMSO, the more significant the presence of free water. Additionally, an increase in the quantity of free water correlates with a decrease in the rigidity of the hydrogen bond network, thus a more substantial decline in HER activity indicates a weaker H-bond network.

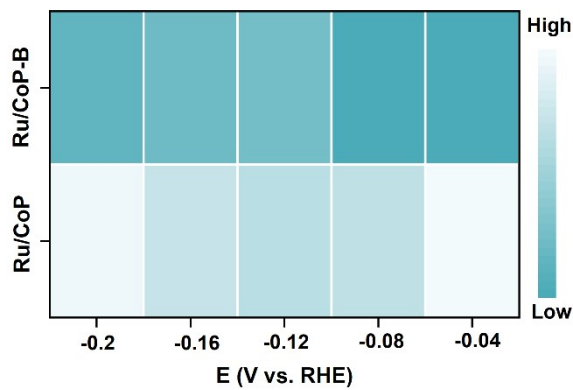


Fig. S52. Raman intensity of  $K^+ \cdot H_2O$  for Ru/CoP and Ru/CoP-B.

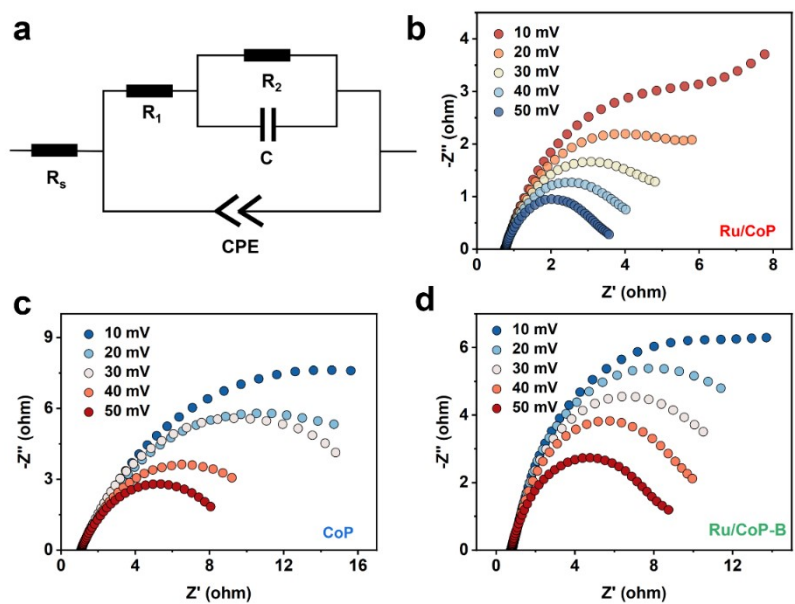
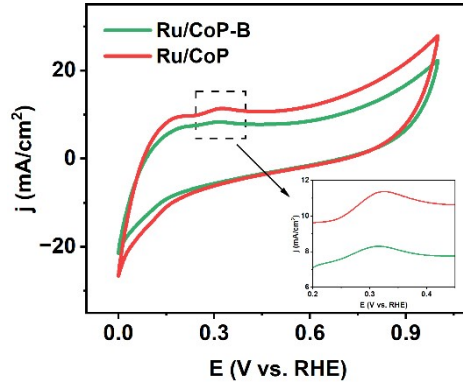
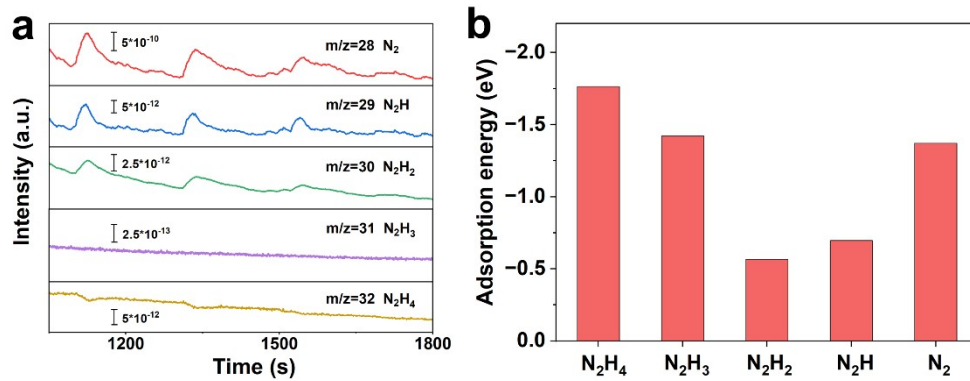


Fig. S53. (a) Schematic diagram of equivalent circuit. EIS plots at different overpotentials of (b) Ru/CoP, (c) CoP, and (d) Ru/CoP-B.



**Fig. S54.** CV curves of Ru/CoP and Ru/CoP-B.

As shown in Fig. S54, Ru/CoP exhibits a larger hydrogen desorption peak compared to Ru/CoP-B, indicating the more \*H produced in Ru/CoP. But notably, there is no H desorption peak observed in CoP.



**Fig. S55.** (a) In-situ DEMS patterns of Ru/CoP. (b) Adsorption energy of different intermediates for Ru/CoP.

The mass-to-charge ratio ( $m/z$ ) signals of 32, 31, 30, 29, and 28 corresponded to the intermediates  $N_2H_4$ ,  $N_2H_3$ ,  $N_2H_2$ ,  $N_2H$ , and  $N_2$ , respectively. There is no peak corresponding to  $N_2H_3$  was detected in all three cycles, which is possibly attributed to the strong adsorption of  $N_2H_3$  during the HzOR process. As shown in Fig. S55b, we found that  $N_2H_3$  exhibited stronger adsorption than  $N_2H_2$ ,  $N_2H$ , and  $N_2$ , which supports our proposed speculation.

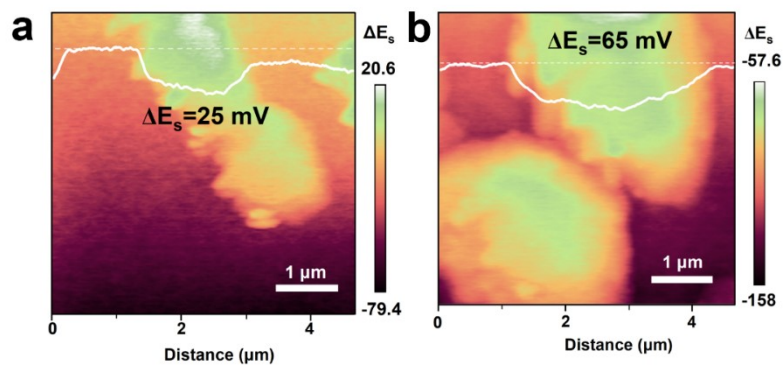


**Fig. S56.** KPFM image of (a) CoP and (b) Ru/CoP-B.

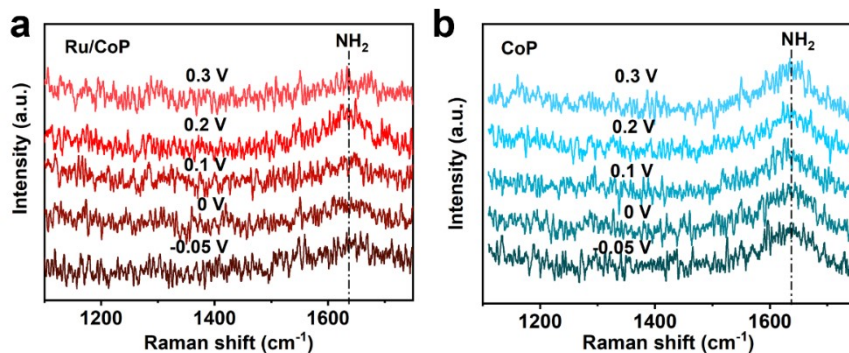


**Fig. S57.** In-situ Raman spectra in 1.0 M KOH and 0.03 M N<sub>2</sub>H<sub>4</sub> of (a) Ru/CoP and (b) CoP.

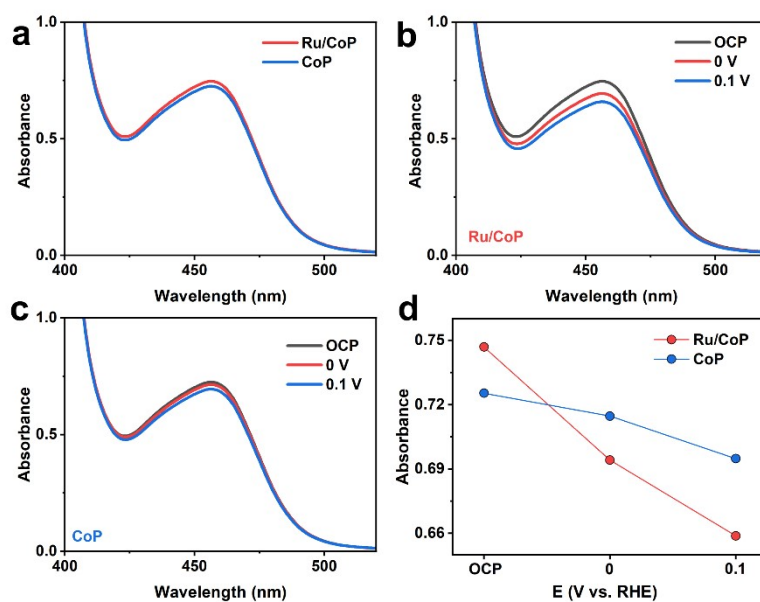


**Fig. S58.** (a) UV-Vis absorbance spectra of N<sub>2</sub>H<sub>4</sub> adsorbed on Ru/CoP and CoP at OCP. UV-vis absorbance spectra of N<sub>2</sub>H<sub>4</sub> adsorbed on (b) Ru/CoP and (c) CoP at different potential. (d) Variation of absorbance of Ru/CoP and CoP under different potentials.

As shown in Fig. S58a, the higher absorbance of Ru/CoP indicates its superiority in N<sub>2</sub>H<sub>4</sub> adsorption at OCP. When tested at 0 and 0.1 V (Figs. S58b and S58c), the decrease in N<sub>2</sub>H<sub>4</sub> absorbance with increasing potential is presumably due to dehydrogenation. The rapid decline in N<sub>2</sub>H<sub>4</sub> absorbance on Ru/CoP compared to CoP further confirms that the built-in electric field enhances N<sub>2</sub>H<sub>4</sub> dehydrogenation (Fig. S58d).

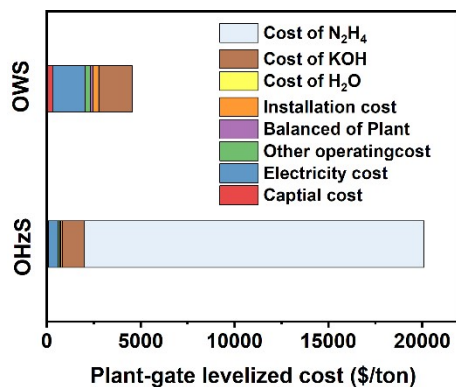


Fig. S59. TEA of OWS system and OHzS system considering raw material cost.

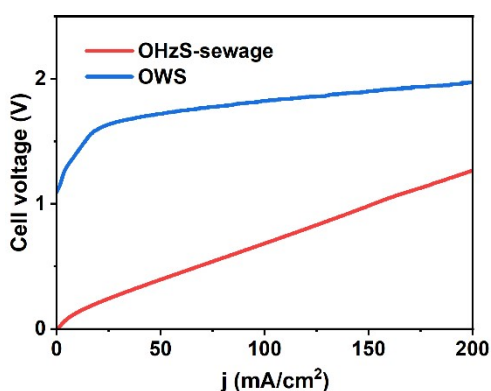


Fig. S60. LSV curves of OWS system and OHzS system using simulated N<sub>2</sub>H<sub>4</sub> sewage (96 ppm).

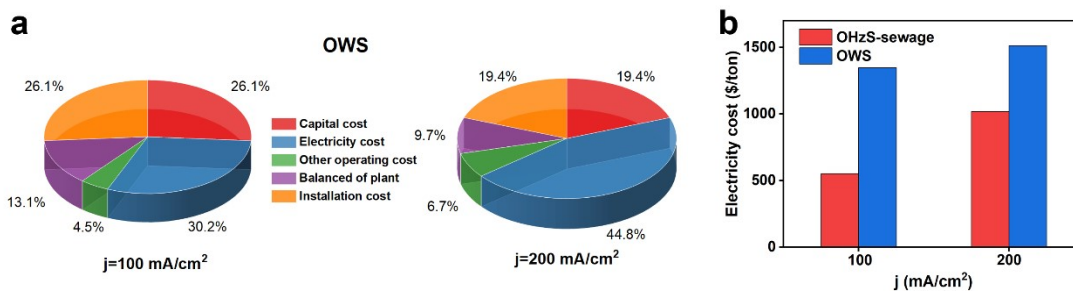
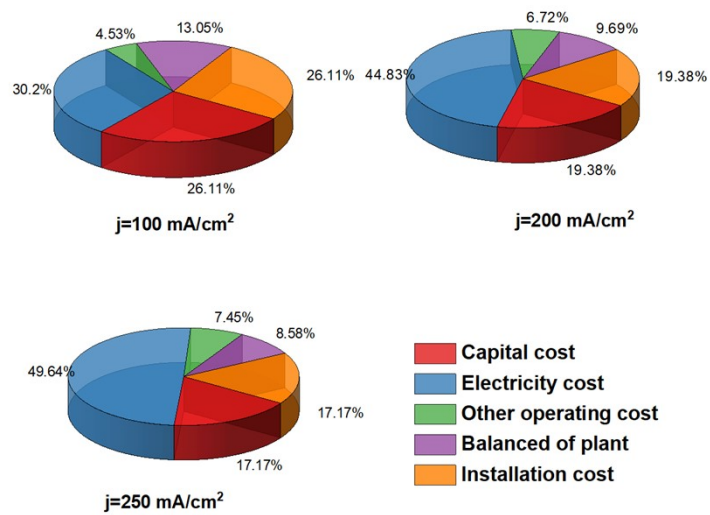


Fig. S61. (a) Various production cost ratios under different current densities in OWS system. (b) Comparison of electricity cost between OWS and OHzS-sewage systems.

As shown in Fig. S61a, electricity cost becomes the primary factor affecting the cost of the OWS system as the voltage increases. In contrast, as depicted in Fig. S61b, the OHzS-sewage system can greatly reduce the electricity cost.



**Fig. S62.** Various production cost ratios under different current densities.

As shown in Fig. S62, the proportion of power consumption in the total cost of hydrogen production also rises as the current density increases.

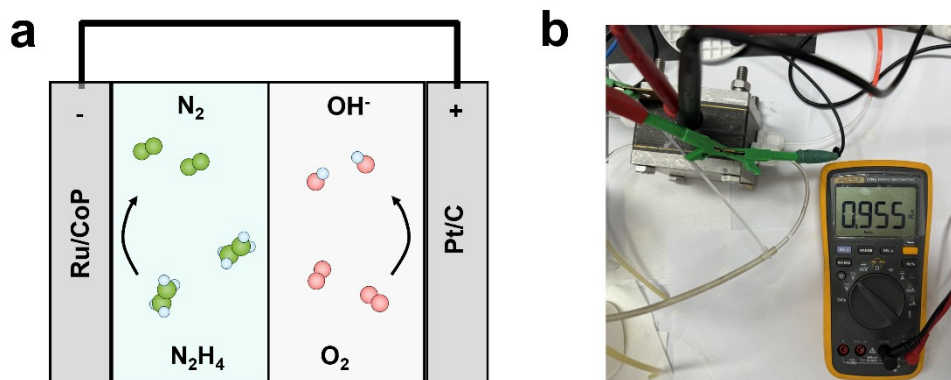


**Fig. S63.** (a) Schematic diagram and (b) picture of DHzFC.

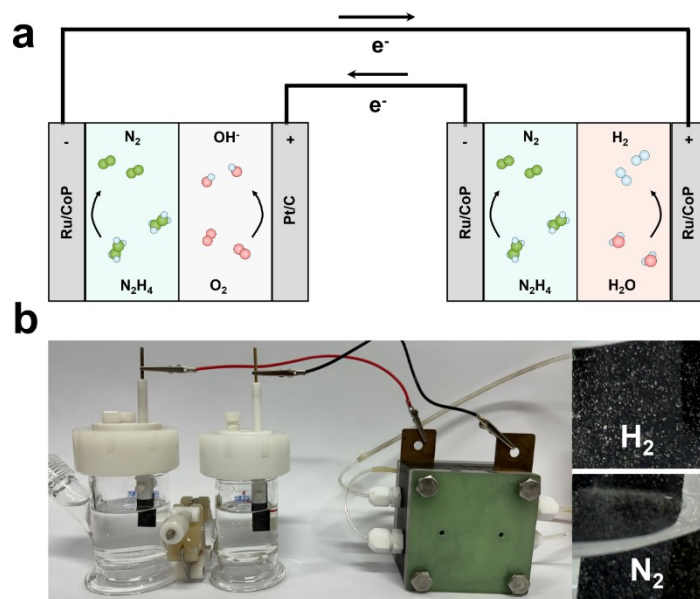


**Fig. S64.** (a) Schematic diagram and (b) picture of self-powered hydrogen production system.

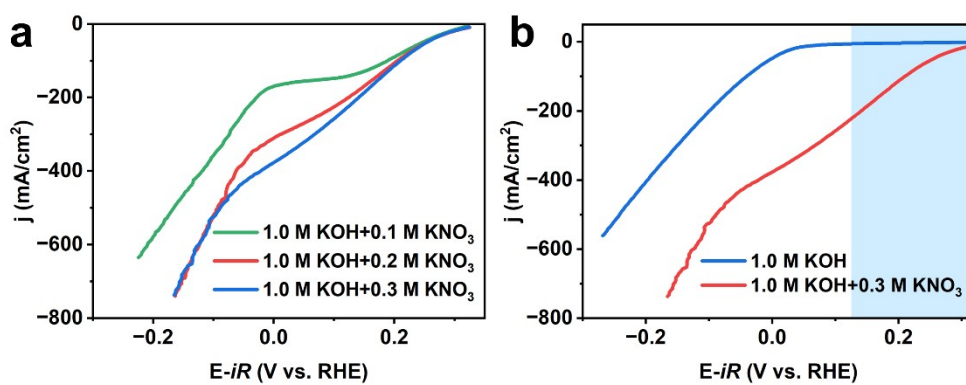


**Fig. S65.** (a) LSV curves of Ru/CoP in 1.0 M KOH with different concentration of  $\text{KNO}_3$ . (b) LSV curves of Ru/CoP in 1.0 M KOH with and without  $\text{KNO}_3$ .

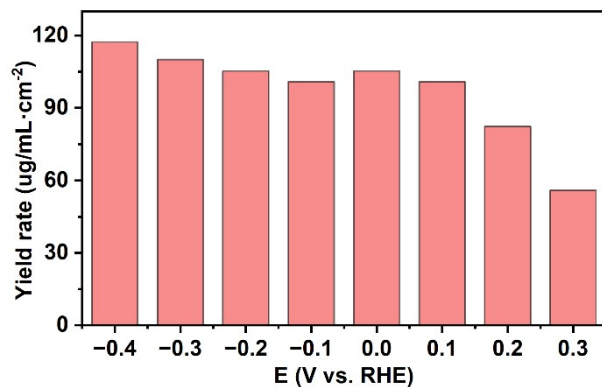


**Fig. S66.** NH<sub>3</sub> yield rates at each given potential.

As shown in Fig. S66, Ru/CoP also exhibits NO<sub>3</sub>RR activity, and its yield rate could reach 117  $\mu\text{g h}^{-1}\text{cm}^{-2}$  at -0.4 V.

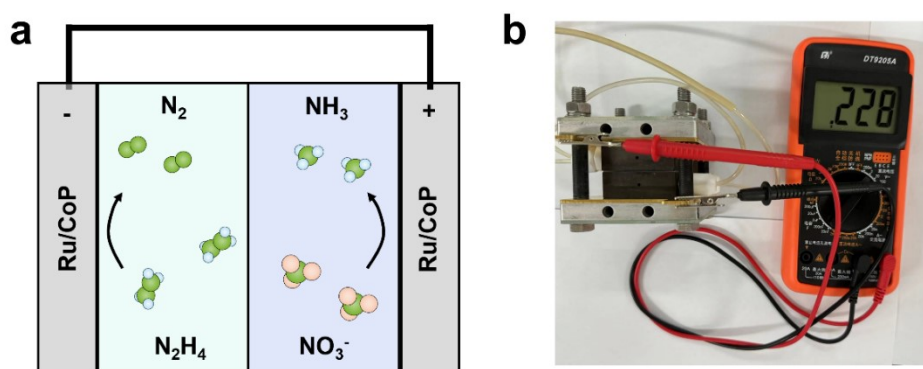


**Fig. S67.** (a) Schematic diagram and (b) picture of hydrazine-nitrate battery.

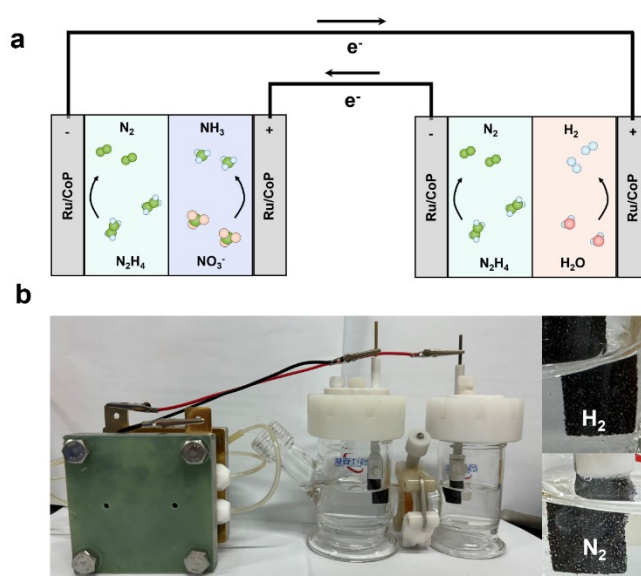


**Fig. S68.** (a) Schematic diagram and (b) picture of hydrazine-nitrate battery powered OHzS system.



**Fig. S69.** Picture of solar-driven OHzS system.

As shown in Fig. S69, we prepared a sample with an area of 3 cm×4 cm by the same methods and assembled a solar-driven hydrazine-assisted hydrogen production system. The power of the solar panel is 5 W, and the theoretical output voltage is 18 V. Here we use the power buck converter to keep the output voltage at 3 V.

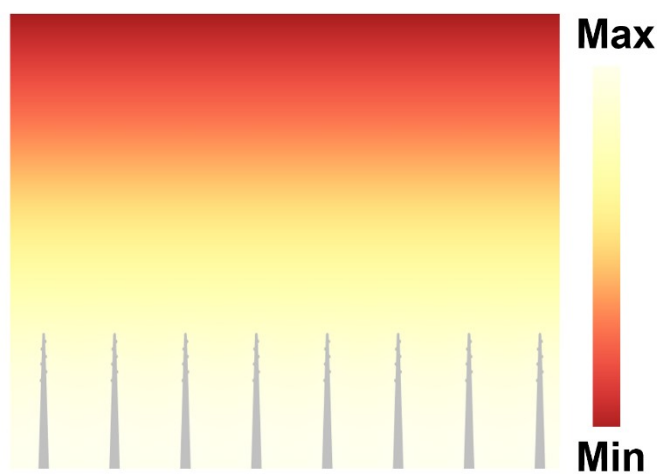


**Fig. S70.** Temperature distribution for Ru/CoP via FEM modeling.

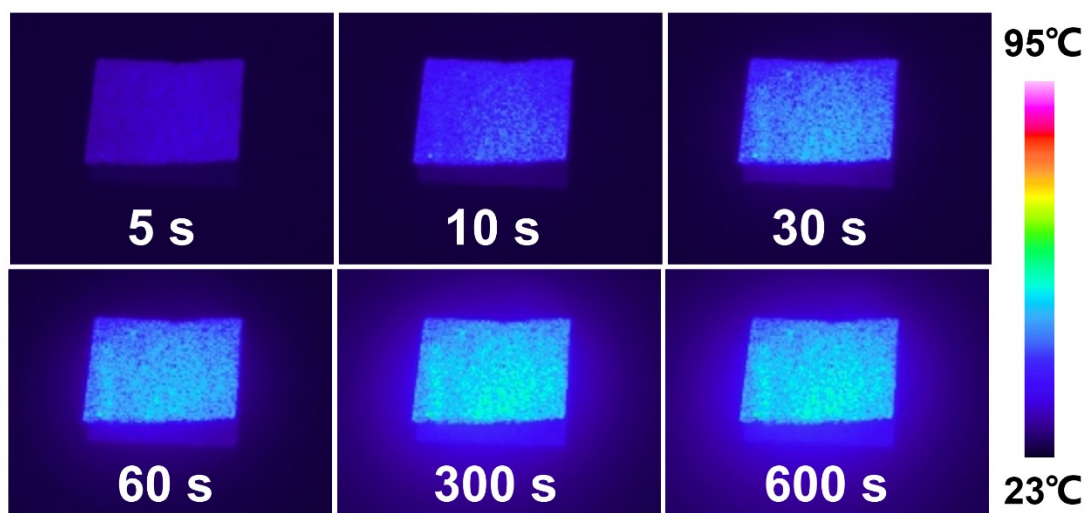


**Fig. S71.** The temperature changes of nickel foam with different times under 808 nm laser.

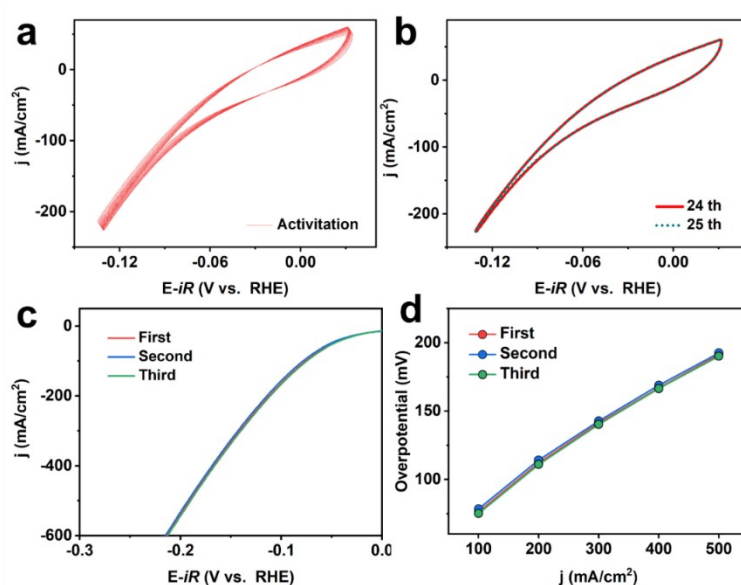


**Fig. S72.** (a) CV activation curves before LSV measurement. (b) 24th and 25th CV curves during CV activation. (c) LSV curves and (d) Overpotential at different current density of the first three times after CV activation.

To verify the existence of the photothermal effect, we conducted a rigorous analysis of our data. Specifically, we performed 25 CV activations, exhibiting that the CV curves of the 24th and 25th activations are nearly coincident (Supplementary Fig. S72a and S72b). Prior to testing the photothermal effect, we conducted three LSV tests. As illustrated in Fig. S72c and S72d, the activity of Ru/CoP remained largely unchanged during these initial tests. Therefore, we can conclude that the observed changes in activity following light irradiation are attributable to the photothermal effect rather than other factors.

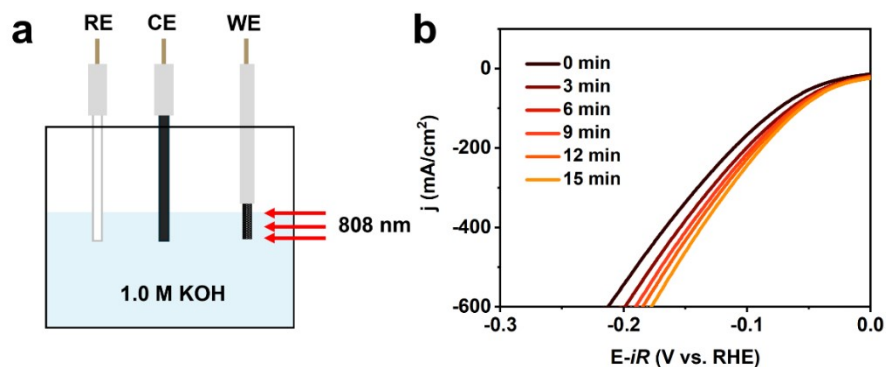


**Fig. S73.** (a) Schematic diagram of photothermal effect test. (b) LSV curves of Ru/CoP with 808 nm irradiation at different times.

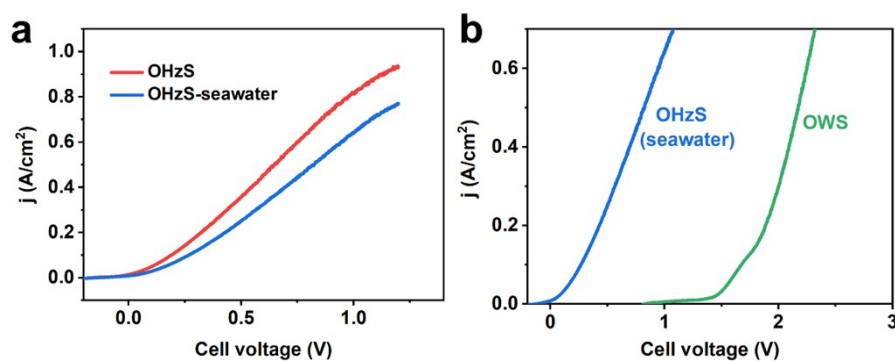


**Fig. S74.** LSV curves of (a) OHzS system used pure water as solvent and OHzS used seawater as solvent. LSV curves of (b) OWS system used pure water as solvent and OHzS used seawater as solvent.

In this experiment, we use simulated seawater as the solvent for the electrolyte of cathode and anode, and the simulated seawater is prepared by adding 0.5 M NaCl into pure water. As shown in Fig. S74, the activity of simulated seawater electrolysis to produce hydrogen is lower compared with OHzS system, but it is still higher than the traditional OWS system.

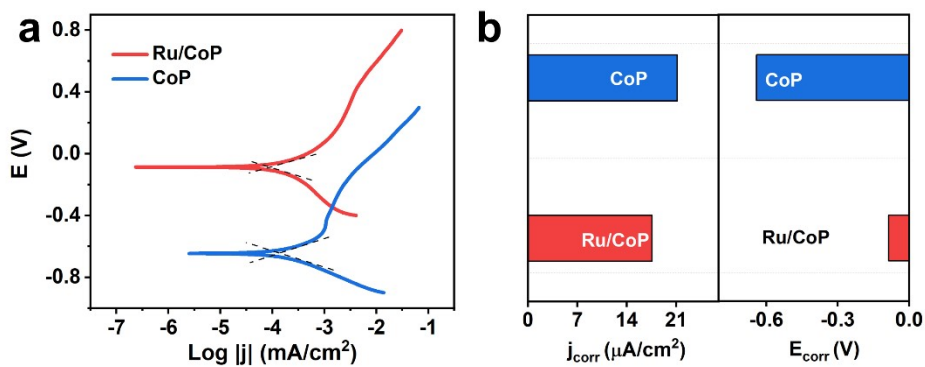


**Fig. S75.** (a) Tafel plots and (b) Corrosion current and corrosion voltage of Ru/CoP and CoP.

Here we consider the corrosion of chloride ions in seawater to electrocatalysts, and the corrosivity test was carried out in 0.5 M NaCl solution. As shown in Fig. S75, compared with NF, Ru/CoP shows a smaller corrosion voltage, indicating that it has good corrosion resistance.

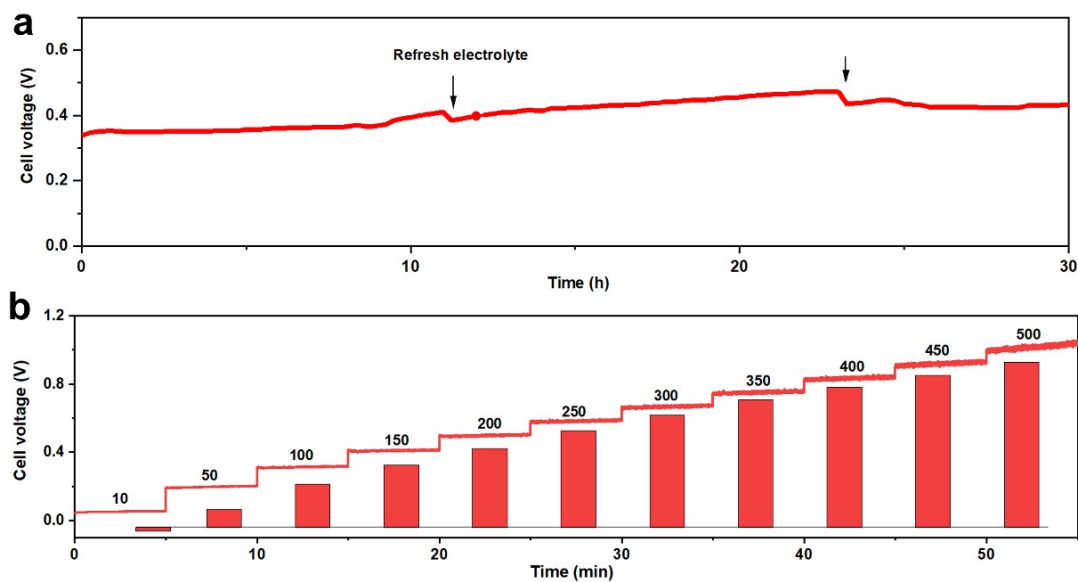


**Fig. S76.** Stability test of Ru/CoP for OHzS system in seawater. (a) Change of cell voltage with time. (b) Cell voltage at different current density.

**Table S1.** Comparison of HER activity of different electrocatalysts

Electrocatalyst	j (mA/cm <sup>2</sup> )	$\eta$ (mV)	Electrolyte	Reference
Y <sub>2</sub> Co-CeO <sub>2</sub>	100	101.0	1.0 M KOH	13
Cu-Ru/RuSe <sub>2</sub>	100	109.0	1.0 M KOH	14
n-Co <sub>3</sub> S <sub>4</sub> @NF	400	311.0	1.0 M KOH	15
RuNi/NC	100	66.0	1.0 M KOH	16
CC@ CoNC-600	100	264.0	1.0 M KOH	4
RuCu-CAT/ CF	100	55.0	1.0 M KOH	17
NA-Ru <sub>3</sub> Ni	100	21.7	1.0 M KOH	18
Pt-NiCoP@MXene	500	181.6	1.0 M KOH	19
CC@WS <sub>2</sub> /Ru-450	100	107.3	1.0 M KOH	20
NiCoP/NF	100	142.0	1.0 M KOH	21
CoO/Mo <sub>2</sub> C	100	285.0	1.0 M KOH	22
WS <sub>2</sub> superstructure	500	205.0	1.0 M KOH	23
Co-P <sub>2</sub> N <sub>2</sub> -C	100	132.0	1.0 M KOH	24
B-MoSe <sub>2</sub>	100	190.5	1.0 M KOH	25
Ni(OH) <sub>2</sub> @Ni-N/Ni-C/NF	100	141	1.0 M KOH	26
Ru/CoP	100	98	1.0 M KOH	This work
Ru/CoP	500	187	1.0 M KOH	This work

**Table S2.** Comparison of HzOR activity of different electrocatalysts.

Electrocatalyst	j (mA/cm <sup>2</sup> )	$\eta$ (mV)	Reference
RP-CPM	500	314	3
RuCo	100	-31	27
NiCo@C/MXene/CF	100	-25	28
Co <sub>0.5</sub> NiS-NSs/NF	100	340	29
WP/NF	10	24	30
PtAgBiTe/C	500	300	31
Ru <sub>1</sub> -NiCoP	500	104	32
FeNiP-NPHC	100	-7	33
CoFeNiCrMnP/NF	100	268	34
Ru-Cu <sub>2</sub> O/CF	100	-13	35
Ru/PNC	255	200	36
Rh-Rh <sub>2</sub> O <sub>3</sub> /C-400	100	56	37
FHNNP/NF	100	44	38
RuCoO <sub>x</sub> @NC	106.9	200	39
Ni(OH) <sub>2</sub> /Ni <sub>2</sub> P/NF	100	73.9	40
Ru/CoP	100	-17	This work
Ru/CoP	500	104	This work

## References

1. C. C. L. McCrory, S. Jung, J. C. Peters and T. F. Jaramillo, *J. Am. Chem. Soc.*, 2013, **135**, 16977-16987.
2. P. Connor, J. Schuch, B. Kaiser and W. Jaegermann, *Z. Phys. Chem.*, 2020, **234**, 979-994.
3. Y. Li, J. Zhang, Y. Liu, Q. Qian, Z. Li, Y. Zhu and G. Zhang, *Sci. Adv.*, 2020, **6**, eabb4197.
4. Y. Xin, K. Shen, T. Guo, L. Chen and Y. Li, *Small*, 2023, **19**, 2300019.
5. X. Wang, J. Xie, S. Li, Z. Yuan, Y. Sun, X. Gao, Z. Tang, H. Zhang, J. Li, S. Wang, Z. Yang and Y.-M. Yan, *Appl. Catal. B Environ. Energy*, 2023, **339**, 123126.
6. X. Wang, S. Li, Z. Yuan, Y. Sun, Z. Tang, X. Gao, H. Zhang, J. Li, S. Wang, D. Yang, J. Xie, Z. Yang and Y.-M. Yan, *Angew. Chem. Int. Ed.*, 2023, **135**, e202303794.
7. P. Ye, K. Fang, H. Wang, Y. Wang, H. Huang, C. Mo, J. Ning and Y. Hu, *Nat. Commun.*, 2024, **15**, 1012.
8. S. Li, X. Wang, X. Chi, Y. Xiong, Y. Sun, Z. Tang, X. Gao, H. Zhang, J. Li, K. Nie, J. Xie, Z. Yang and Y.-M. Yan, *Adv. Funct. Mater.*, 2023, **33**, 2306098.
9. Y. Gu, B. Xi, W. Tian, H. Zhang, Q. Fu and S. Xiong, *Adv. Mater.*, 2021, **33**, 2100429.
10. C. Fettkenhauer, X. Wang, K. Kailasam, M. Antonietti and D. Dontsova, *J. Mater. Chem. A*, 2015, **3**, 21227.
11. A. E. Kisa and O. Demircan, *J. Solid State Electrochem.*, 2024, **28**, 12785-1798.
12. R.-T. Gao, L. Liu, Y. Li, Y. Yang, J. He, X. Liu, X. Zhang, L. Wang and L. Wu, *Proc. Natl. Acad. Sci. U.S.A.*, 2023, **120**, e2300493120
13. X. Liu, S. Wei, S. Cao, Y. Zhang, W. Xue, Y. Wang, G. Liu and J. Li, *Adv. Mater.*, 2024, **36**, 2405970.
14. K. Wang, J. Zhou, M. Sun, F. Lin, B. Huang, F. Lv, L. Zeng, Q. Zhang, L. Gu, M. Luo and S. Guo, *Adv. Mater.*, 2023, **35**, 2300980.
15. T.g Li, B. Wang, Y. Cao, Z. Liu, S. Wang, Q. Zhang, J. Sun and G. Zhou, *Adv. Mater.*, 2023, **35**, 2300980.
16. L. Zhang, H. Hu, Ch. Sun, D. Xiao, H.-T. Wang, Y. Xiao, S. Zhao, K. H. Chen, W.-X. Lin, Y.-C. Shao, X. Wang, C.-W. Pao and L. Han, *Nat. Commun.*, 2024, **15**, 7179.
17. Y. He, Z. Ma, F. Yan, C. Zhu, T. Shen, S. Chou, X. Zhang and Y. Chen, *Proc. Natl. Acad. Sci. U.S.A.*, 2024, **121**, e2320777121.
18. L. Gao, F. Bao, X. Tan, M. Li, Z. Shen, X. Chen, Z. Tang, W. Lai, Y. Lu, P. Huang, C. Ma, S. C. Smith, Z. Ye, Z. Hu and H. Huang, *Proc. Natl. Acad. Sci. U.S.A.*, 2024, **121**, e2320777121.
19. H.-J. Niu, C. Huang, T. Sun, Z. Fang, X. Ke, R. Zhang, N. Ran, J. Wu, J. Liu and W. Zhou, *Angew. Chem. Int. Ed.*, 2024, **63**, e202401819.
20. J. Li, Y. Li, J. Wang, C. Zhang, H. Ma, C. Zhu, D. Fan, Z. Guo, M. Xu, Y. Wang and H. Ma, *Angew. Chem. Int. Ed.*, 2024, **63**, e202401819.
21. H.-Y. Wang, L. Wang, J.-T. Ren, W. Tian, M. Sun, Y. Feng and Z.-Y. Yuan, *ACS Nano*, 2023, **17**, 10965-10975.
22. H.-Y. Chen, L. Yang, R.-X. Wang, W.-J. Zhang, R. Liu, Y.-Z. Yun, N. Wang, S. Ramakrishna, L. Jiao and Y.-Z. Long, *Small*, 2023, **19**, 2304086.
23. L. Xie, L. Wang, X. Liu, J. Chen, X. Wen, W. Zhao, S. Liu and Q. Zhao, *Nat. Commun.*, 2024, **15**, 5702.
24. S. Qian, F. Xu, Y. Fan, N. Cheng, H. Xue, Y. Yuan, R. Gautier, T. Jiang and J. Tian, *Nat. Commun.*, 2024, **15**, 2774.

25. T. Zhang, Q. Ye, Z. Han, Q. Liu, Y. Liu, D. Wu and H. J. Fan, *Nat. Commun.*, 2024, **15**, 6508.
26. K. Dastafkan, X. Shen, R. K. Hocking, Q. Meyer and C. Zhao, *Nat. Commun.*, 2023, **14**, 547.
27. W. Zhu, X. Zhang, F. Yao, R. Huang, Y. Chen, C. Chen, J. Fei, Y. Chen, Z. Wang and H. Liang, *Angew. Chem.*, 2023, **135**, e202300390
28. F. Sun, J. Qin, Z. Wang, M. Yu, X. Wu, X. Sun and J. Qiu, *Angew. Chem.*, 2023, **135**, e202300390.
29. X.-H. Wang, R. Yuan, S.-B. Yin, Q.-L. Hong, Q.-G. Zhai, Y.-C. Jiang, Y. Chen and S.-N. Li, *Adv. Funct. Mater.*, 2023, **34**, 2310288.
30. C. Lim, H. Roh, E. H. Kim, H. Kim, T. Park, D. Lee and K. Yong, *Adv. Funct. Mater.*, 2023, **34**, 2310288.
31. F. Zhao, S. Nie, L. Wu, Q. Yuan and X. Wang, *Adv. Mater.*, 2023, **35**, 2303672.
32. Y. Hu, T. Chao, Y. Li, P. Liu, T. Zhao, G. Yu, C. Chen, X. Liang, H. Jin, S. Niu, W. Chen, D. Wang and Y. Li, *Angew. Chem.*, 2023, **135**, e202308800.
33. Q. Yu, X. Liu, G. Liu, X. Wang, Z. Li, B. Li, Z. Wu and L. Wang, *Adv. Funct. Mater.*, 2022, **32**, 2205767.
34. K. Li, J. He, X. Guan, Y. Tong, Y. Ye, L. Chen and P. Chen, *Small*, 2023, **19**, 2302130.
35. P. Shen, B. Zhou, Z. Chen, W. Xiao, Y. Fu, J. Wan, Z. Wu and L. Wang, *Appl. Catal. B Environ. Energy*, 2023, **325**, 122305.
36. X. Guan, Q. Wu, H. Li, S. Zeng, Q. Yao, R. Li, H. Chen, Y. Zheng and K. Qu, *Appl. Catal. B Environ. Energy*, 2023, **323**, 122145.
37. J. Gao, W. Yu, J. Liu, L. Qin, H. Cheng, X. Cui and L. Jiang, *J. Colloid Interface Sci.*, 2024, **664**, 766-778.
38. S. Zhang, X. Wei, S. Dai, H. Wang and M. Huang, *Adv. Funct. Mater.*, 2024, **34**, 2311370.
39. R. A. Senthil, S. Jung, A. Min, C. J. Moon and M. Y. Choi, *Chem. Eng. J.*, 2023, **475**, 146441.
40. H.-M. Yang, H.-Y. Wang, M.-L. Sun and Z.-Y. Yuan, *Chem. Eng. J.*, 2023, **475**, 146134.